Basement fault trends in the Southern North Sea Basin

Anna Dorota PREISS*[a], Jürgen ADAM[a]

[a]Department of Earth Sciences, Royal Holloway, University of London, Egham Hill, Egham, Surrey TW20 0EX

anna.preiss.2017@live.rhul.ac.uk, Tel. +48 574 170 716

jurgen.adam@rhul.ac.uk

Keywords: Zechstein salt, fault mapping, seismic attributes, Southern North Sea, fault trend analysis

The Southern North Sea Basin (SNS) contains the regional Zechstein megahalite, a highly deformed Upper Permian salt layer, which partly obscures the Palaeozoic basement structures. This study provides a comprehensive and systematic analysis of pre-salt basement fault trends in the SNS mapped at the top Rotliegend level. We utilise a consistent fault mapping methodology with seismic attribute-based fault mapping techniques and GIS-based image tracing. The results are compared with published maps from the Southern North Sea area. Data analysis is performed on a supra-regional time-migrated 3D seismic dataset located offshore Netherlands and the United Kingdom. Statistical directional analysis of fault trends in the study area confirms the published dominant NW-SE basement trend and allows quantifying its contribution at approximately 51% of all fault segments. Basement fault trend distributions in individual sub-basins in the SW SNS are highly similar and show a strong NW-SE trend dominance despite different tectonic histories of those sub-basins. This may imply their joint origin prior to Caledonian accretion of the Laurussian continent. In the NE sub-basins, NE-SW, W-E and N-S trends are locally important and may represent the structural inheritance of smaller pre-Caledonian terranes.

1. Structural trends in the Southern North Sea Basin

Despite nearly 60-years of exploration in the Southern North Sea Basin, our understanding of its geological history and internal structure is still not complete. Salt tectonic processes acting in the basin throughout most of the Mesozoic and Cenozoic times in different tectonic regimes, strongly contributed to a high level of structural complexity of the post-salt basin fill. The presence of a highly deformed salt layer and, in particular, salt diapirs and salt walls in many areas of the basin, hinders the interpretation of the underlying basement by completely obscuring the pre-salt reflectors in some areas. This is well depicted in Figure. 1 c, where salt structures produce velocity pull-ups and distortion of the reflector at the base-of-salt horizon, making interpretation of pre-salt horizons difficult. Despite the challenge, many authors have made attempts to provide a clear view on the distribution of basement trends and major faults in the Southern North Sea. Stewart and Coward (1995), basing their study on 2D seismic data from the UK sector, highlighted four major structural trends present in the Southern North Sea basement (Fig. 1 a), with the dominant NW-SE direction and NE-SW, S-N and W-E trends important more locally across the basin. Especially the semi-continuous and parallel NE-SW trend, in the literature referred to as 'Dekeyser' faults (Ojik et al., 2019), is of high importance for compartmentalization of Rotliegend hydrocarbon reservoir intervals.

In regional studies (e.g. Duin et al., 2006, Peryt et al., 2010, ten Veen et al., 2012) there is a natural tendency to simplify the observed fault patterns to dominant trends and basin-bounding faults (Fig. 1 d). More detailed studies carried out to date were either based largely on 2D seismic datasets acquired perpendicular to the main basement trends, thus directionally biased (e.g. Oudmayer and De Jager, 1993) or despite detailed structural interpretation and trend analysis, they were focused more locally and did not cover the full extent of the SNS basin (e.g. de Jager, 2007). To better understand regional fault trend changes and the importance of differently oriented fault systems in various areas of the basin, a more complete regional fault trend dataset is required. Locally conducted studies highlighting basement structure with the use of seismic attributes (Harding and Huuse, 2015, Ojik et al., 2019) show that in the presence of 3D seismic data, detailed mapping of the pre-salt basement can be successfully obtained through attribute analysis. Fault maps obtained from attribute analysis on 3D seismic data, as opposed to 2D seismic, are not biased by the direction of acquisition, scale of observation and subjective choices done by the interpreter. Therefore, such maps should be the most suitable input for a comprehensive regional structural trend analysis. This study attempts to utilize existing attribute-based fault mapping techniques combined with GIS-based image tracing to extract fault trend information from a supra-regional 3D seismic dataset in the Southern North Sea and perform a spatially consistent fault trend analysis across its sub-basins.

Figure 1 here

2. Regional setting

2.1. Basement framework of the Southern North Sea Basin

The history of the Southern North Sea Basin can be tracked back to Proterozoic however, the present-day architecture of the basin is deeply rooted in Paleozoic tectonic events that led to progressive accretion of the basement and establishment of the tectonic grain.

The first one of those events was the Ordovician-Silurian collision between two continental plates, Laurentia and Baltica and the Avalonia composite continental terrane derived from Gondwana (Pharaoh, 1999). The Laurussian continent and Caledonian fold belts were formed as a result of this collision. The present-day area of the Southern North Sea Basin almost entirely lies within the Avalonia terrane and only partly in Baltica. The NW-SE structural grain in the Palaeozoic basement of the North Sea, more or less parallel to the Avalonia-Baltica suture zone is probably directly inherited from this collision (de Jager, 2007) although it is also believed it may have originated from a pre-collision stage (Stewart and Coward, 1995). The W-E to WNW-ESE trend present more locally in the SNS basement is also believed to have a Caledonian origin (Ziegler, 1990a). Similar trends can be observed onshore NE Netherlands and are known from the Lower Saxony Basin (de Jager, 2007).

Figure 2 here

The second event is related to the convergence between Laurussia and Gondwana continents, which was initiated during the Devonian and culminated in continental collision and thin-skinned thrusting with c. 300 km of shortening in the Rheno-Hercynian Zone during the late Visean and Westphalian D times (Oncken et al., 2000), south of the North Sea. A flexural foreland basin, which formed North of the Variscan deformation front, was eventually inverted in Late Stephanian times. The evidence of inversion can be found as far north as Central England. It is believed that despite peripheral position of the North Sea to the Variscan orogen, the processes within the orogen had a strong effect on the tectonic evolution in this area (Besly, 1998). During this time probably the NNW-SSE basement trend was established in the eastern Netherlands along a Devonian seeway in the area of the present-day Dutch Central Graben (Ziegler, 1990a, Oudmayer and De Jager, 1993, de Jager, 2007). The NE-SW trend is known from sinistral strike-slip faulting during the Acadian orogenic event in Devonian that preceded the Variscan Orogeny (Stewart and Coward, 1995).

At the Carboniferous/Permian boundary, the Southern North Sea and surrounding areas were transected by a system of post-orogenic conjugate strike-slip faults, which utilized NW-SE Caledonian lineaments (Glennie, 1990, Ziegler, 1990b). Some of these faults are known to be boundaries of sub-basins in the Southern North Sea, as depicted in Figure. 2.

Throughout the Mesozoic-Cenozoic history of the SNS the Caledonian and Variscan faults were subsequently reactivated in various tectonic regimes and regional stress orientations, which was generally not at right angles to the existing structures. This resulted in predominantly oblique-slip along the fault planes and consequently, very high parallelism and length-to-throw ratios (Oudmayer and De Jager, 1993). The evidence for this re-activation can be found at younger stratigraphic horizons, where post-salt faults tend to be oriented in the same direction as the basement faults or they create an en-echelon pattern related to the strike-slip movement along the pre-salt structures. To accommodate the oblique slip, link-up faults developed between the main basement structures, locally forming narrow pop-ups or slight doming in the overburden but otherwise, post-Paleozoic tectonic events did not have a major effect on the formation of basement structures and new directions of faulting.

The SNS essentially consists of several sub-basins (Fig. 2), which originated from intra-plate Permo-Triassic extension that followed the Variscan Orogeny (Glennie and Underhill, 1998) and which have largely undergone different Mesozoic-Cenozoic tectonic histories. Mid-Jurassic thermal doming and subsequent Upper Jurassic-Lower Cretaceous rifting have different stratigraphic signatures in different sub-basins. Platform areas, such as the Cleaver Bank High, Schill Ground High or Ameland Platform, were uplifted and eroded in response to Upper Jurassic rifting in the Central Graben area and do not carry much stratigraphic record from this period of time as opposed to the surrounding basins, in particular the Central Graben. Upper Cretaceous and Paleogene-Neogene inversion pulses similarly affected only parts of the SNS, such as The Broad Fourteens Basin, Sole Pit High or the southern part of the Central Graben. Nevertheless, the tectonic stresses acting on the basins are believed to have led to selective reactivation of older structures rather than creating new fault systems in the basement (de Jager, 2007). Therefore, different sub-basins in the SNS, despite their different tectonic histories, show strong similarities in structural trends.

2.2. Tectono-stratigraphy

The post-Permian stratigraphic record of the Southern North Sea Basin is only partly preserved and the level of preservation varies widely across neighbouring sub-basins (Fig.2). Of major importance in the stratigraphic record is the Zechstein evaporite layer, which contains significant amounts of halite and has undergone salt tectonic deformation throughout the basin’s tectonic history (magenta layer in Fig. 3). This layer separates the Paleozoic basement from the Mesozoic-Cenozoic overburden and partly decouples the deformation between these two units. The extent of the salt layer in the SNS is shown in Figure 2.

Figure 3 here

Events of regional uplift and inversion have led to the formation of prominent basin-wide angular unconformities in the overburden, which can be traced across the study area and nearly the entire Southern North Sea (Fig. 3). These include the Mid-Cimmerian Unconformity related to thermal doming in mid-Jurassic times and a more recent unconformity related to Alpine inversion, offshore largely overlain by Quaternary sediments.

3. Dataset

The seismic dataset used in this study is a fully time-migrated Southern North Sea MegaSurvey 3D seismic dataset provided by Petroleum Geo-Services (PGS) and the Oil and Gas Authority (OGA). The dataset is a megamerger of numerous smaller 3D seismic surveys varying in size and quality, which were re-processed, corrected for seismic mis-ties and re-organized into 44 3D surveys with unified geometries. Out of 44 available reprocessed 3D surveys, 39 were used for all regional attribute analyses described in the following Methodology section. They cover a total area of over 61 000 km^2 and their extent is shown in Figure 2.

3.1. Data availability

The Southern North Sea MegaSurvey data from the UK sector are available on the National Data Repository webpage at the following address: https://ndr.ogauthority.co.uk.

3.2. Data quality

The quality of the data varies across the study area from fair to excellent and depends on various factors, including among other type of acquisition (in places visibly lower quality onshore vs higher quality offshore) and geological factors such as the structural complexity, the thickness variation of the salt layer and the type of contact between the salt and the surrounding strata (concordant vs. discordant), all of which can have a major effect on the imaging of the reflectors underlying and surrounding salt structures, as shown in Figure 4. These and other characteristics of otherwise generally high-quality seismic data, such as residual mis-ties between merged surveys, any seismic artifacts and acquisition footprint at shallow depths had to be considered, as they could locally affect the results of attribute computation and subsequent trend analysis.

Figure 4 here

4. Methodology

The methodology used in this study combines seismic attribute analysis and automatic raster tracing to detect and map faults at the base-of-Zechstein seismic stratigraphic horizon, locally modified, refined from original interpretation provided by the Petroleum Geo-Services and gridded. A TWT map of the base-of-Zechstein horizon is shown in Figure 5.

Figure 5 here

4.1. Attribute-based fault mapping techniques

Seismic attributes have been widely used for the last few decades to map structural discontinuities in 3D seismic data. Most commonly used edge detection methods are based on different coherency attributes, which measure the level of similarity between traces and the continuity of the waveform (Chopra and Marfurt, 2007). These methods have proven valuable tools for detecting discontinuities and were widely described in the literature in 1990s (e.g. Bahorich and Farmer, 1995, Marfurt et al., 1998, Gersztenkorn and Marfurt, 1999). Coherency computations can be based on several estimations, including cross-correlation, semblance, variance, least squares, eigenstructure or gradient structure tensor. All of these algorithms are sensitive to structural dip and should be computed taking into account the reflector dip. They operate on various numbers of adjacent traces, from 3 for the most basic cross-correlation to 9 and more traces for more advanced methods, as well as on a specified analysis time window, both of which have a strong impact on the horizontal and vertical resolution of seismic structural and stratigraphic features detected in the 3D data. For structural discontinuities, Marfurt et al. (1998) in their paper showed that increasing the analysis time window for semblance-based coherency attribute improves the horizontal resolution of structural features in the seismic data, especially for high-angle faults, at a cost of vertical resolution and improves S/N ratio. Similarly, using a higher number of adjacent traces for analysis, improves the S/N ratio however it requires more computational power. Both semblance- and variance-based coherency are sensitive to amplitude variations between traces. The eigenvalue-based algorithm, described in detail by Gersztenkorn and Marfurt (1999) provides the best lateral resolution and it is amplitude-insensitive however, it is also the most computationally intensive. With the computing capabilities of present-day workstations such limitations are becoming less significant even for large seismic datasets.

The beginning of the new century has seen a rise of more advanced techniques, developed to enhance the faults and reduce content of noise in coherency volumes by use of directional filters, ant tracking and image recognition algorithms (Chopra and Marfurt, 2007). They should be especially handy in areas where the level on background noise in the coherency cube does not allow to easily trace structural discontinuities, as in the case of faults underlying deformed salt layers. Some of those algorithms were adopted in different commercial software packages (e.g. ant tracking in Petrel (™Schlumberger) or i3D – image recognition technique, in Kingdom (™IHS Markit)). They allow extraction of fault surfaces or fracture networks from coherency attribute volumes, where vertical continuity of faults and data quality are sufficient. In the literature ant tracking and its modifications were mostly utilized by various authors to characterize fault networks in fractured and faulted reservoirs (e.g. Laake et al., 2011, Antrett et al., 2012, Tamagawa et al., 2012).

While fault enhancement techniques are commercially available on local workstations, they require a good computing power for efficient calculations and visualization and can be challenging to handle for large seismic datasets. Additionally, for large volumes of 3D seismic data and variable data quality, fault extraction and especially quality control of results may become very time consuming.

Fault enhancement and extraction does not need to be based on coherency attributes. Some authors propose alternative algorithms, which compute the likelihood of the fault surface at a given point in the seismic data volume (e.g. Cohen et al., 2006, Hale, 2012). Recently, with the exponential progress in digitalization of the geoscience world, machine-learning fault-detection techniques, largely requiring access to high-performance computing (HPC) infrastructure, have been given a lot of attention. These techniques may be fully automatic or based on a training fault interpretation sample provided by the interpreter, which is used by the algorithm to learn the definition of structural discontinuities and apply it on the entire seismic volume to detect the faults. These techniques will not be further discussed in this paper. Some examples can be found in Wu et al. (2019) and Ashraf et al. (2020).

4.2. Fault mapping workflow

For the selection of fault detection and enhancement methods to be used in this study a few factors were taken into account to ensure a good quality result with the available tools at hand. These were, in the order of importance:

1. The available standard workstation computing infrastructure
2. Large size of the seismic dataset, which requires long computation time
3. The abundance of published information on the settings and limitations of the algorithms.

Based on the above, we have decided to use semblance-based coherency attributes for fault detection and ant tracking for further enhancement of faults in the seismic image, however a different combination of attributes could be used to provide a similar result. The general mapping process was modified from a workflow proposed by Pedersen et al. (2005) for automatic extraction of fault surfaces from seismic data, using artificial ants, who suggest a three-step process, involving extraction of 3D fault patches as the final step. Due to a very large size of the seismic dataset, viariability in seismic data quality between surveys and a potentially time-consuming quality control process, the extraction of fault patches was substituted with automatic raster tracing of the attribute map in GIS software. Therefore, the results include fault strike directions only, without dip information. The methodology, as depicted in Figure 6, involves three consecutive steps, namely: edge detection, edge enhancement and fault mapping, which will be discussed in the following sections.

Figure 6 here

4.2.1. Edge detection

This step consists in transforming an input 3D seismic amplitude volume into a volume of discontinuities in seismic data. In this study we utilized the similarity attribute (semblance-based attribute) available in the Kingdom software (™ IHS), which extracts information about discontinuities (structural and other boundaries) from a reflection seismic data volume (Brown, 2011). The algorithm uses the semblance coefficient to compare the energies of a given number of traces with the total number of traces in a selected time window. Any deviation from the maximum similarity value may indicate structural or stratigraphic discontinuities.

According to Pedersen et al. (2005), good results for coherency attributes can be obtained by applying a smoothing layer-parallel filter to the input seismic data prior to attribute computation. In this study however, smoothing was obtained synchronously with computation of similarity by applying a large similarity time window (240 ms) in order to attenuate noise and improve the continuity of large faults. As mentioned in the previous section, using a large time window for similarity computation reduces the vertical resolution of the resultant attribute cube. In this case however, attribute computation was focused on obtaining the best possible horizontal resolution that would allow vector tracing the attribute analysis results on a map at a later stage. 7 adjacent traces were used for similarity estimation. The attribute was computed along structural dip to avoid detecting artifacts associated with steeply dipping strata, commonly called “structural leakage”, which can potentially be misinterpreted as faults (Marfurt and Alves, 2015) and which could be mistakenly enhanced in the fault enhancement stage.

As depicted in Figure 1b, the detection of discontinuities in the seismic data may not significantly improve our understanding of fault networks underlying a deformed salt layer, especially underneath salt diapirs and salt walls. Salt velocity pull-ups distort the reflectors underneath the salt, producing noisy “shadow zones”, which mimic in their extent the overlying salt structures and obscure the structural information. To bring out the structural information, the similarity result was enhanced using the ant tracking attribute.

Prior to running the fault enhancement step, all similarity cubes were recalculated by subtraction from a constant value of 1.5 (a contractual maximum value for similarity chosen based on maximum values of all analysed cubes) to allow enhancing discontinuities represented by high attribute values with the ant tracking attribute in the next step.

4.2.2. Edge enhancement

At this stage edge detection result was conditioned using a two-step ant tracking computation process. The inputs for attribute computation in runs 1 and 2 were: similarity cube and ant tracking result from run 1 respectively. The second attribute run is not compulsory but it was performed to provide a sharper image input for automatic raster tracing.

The underlying concept of the ant-colony optimization (ACO) was first introduced by Dorigo et al. (1996). The algorithm iteratively attempts to connect low coherence zones associated with structural events in a way that is analogical to ants following the shortest possible path from their nest to the food source. The higher the number of electronic ants follow a discontinuity, the more pronounced the fault surface will be in the resulting ant track cube (Chopra and Marfurt, 2007). The main characteristic of the ant tracking result, is a bitmap trace of the faults represented by a thin discrete line, which is obtained through an operation called thinning. This operation checks along a line perpendicular to the fault in which voxel along the line the ant tracking value is highest. Only peak values are retained, while other are discarded (Randen et al., 2001). In this study the attribute was computed using increased spacing between electronic ants, which allowed enhancing only large-scale discontinuities.

Fault planes are generally expected to have dips higher than 45°. This is especially true for pre-salt basement in the SNS, where the majority of faults are high-angle features. Therefore, all events having dips lower than 46° were discarded in all azimuth directions (Pedersen et al., 2005). Similarly, processing artefacts and data boundaries produce usually vertical features, which can be filtered out from the entire volume in a specified range of azimuths. Here, to remove any vertical and sub-vertical artefacts along the boundaries of neighbouring seismic surveys, all events trending in the inline and crossline direction with dips between 80° and 90° were filtered out. Additionally, all events dipping 88°-90° were discarded in all azimuth directions, to remove processing artefacts, for example related to mis-ties between original seismic surveys. This allowed obtaining an attribute volume with enhanced geological discontinuities and attenuated artifacts. However, it is important to keep in mind that while filtering allows removing undesired information, this operation may remove some natural sub-vertical discontinuities, which is particularly clear along the edges of the reprocessed surveys, where some part of fault information is missing.

The final attribute map used as input for automatic raster tracing is shown in Figure 7.

4.2.3. Fault mapping

The fault mapping step is realized through automatic raster tracing (also referred to as automatic vectorization) of final ant tracking results extracted on a TWT horizon map. The process uses a Vectorization tool (Esri® ArcMap™ software) (Fig. 5) to generate a set of polylines, which represent fault traces on the horizon map. A detailed workflow illustrating a sequence of steps required to produce such a fault dataset, ready for further statistical analysis, is shown in Figure 6 (bottom). This workflow depicts the transition from step II – fault enhancement to step III – fault mapping in Figure 6 (top).

The input map for automatic vectorization was obtained by extracting the ant tracking attribute on the base-of-Zechstein horizon. The attribute map was then exported as a raster file and imported into ArcMap, where it was spatially referenced and binarized to allow automatic tracing of linear features in the Vectorization tool. The results of the vectorization process are highly dependent on the parameters set by the user. Some important parameters include noise level, gap closure tolerance and fan angle (ArcMap 2014). The first one controls the level of detail retained in the resulting image. The higher the percentage value, the less detail is extracted from the input raster. The level of noise chosen for this operation was set to 75% to assure inclusion of continuous events in the extraction only, without considering chaotic and discontinuous lines. The latter two parameters define the size of a gap in pixels of the raster file across which two lines will be connected and a search angle for detecting a connection. The gap closure tolerance was set to a low value in order to avoid as much as possible random connections between closely spaced parallel lines. The fan angle was set to 60 degrees to avoid false perpendicular connections but improve continuity of curved fault systems. As a result of this process, a set of polylines was produced as shown in Figure 8.

Due to the automatic character of this process, the results needed to be quality checked for consistency with the attribute maps and seismic data as well as presence of any residual artifacts and lineations from inclined strata.

5. Results

5.1. Fault network of the pre-salt section

The intermediate and final results of fault mapping workflow are shown in Figures 7 and 8. No acquisition footprint was detected at the base-of-Zechstein horizon however, a small number of linear seismic artifacts, easy to confirm on seismic sections, were detected and removed from further analysis. Figure 8 shows the final fault map, where artifacts have been removed. Regularly spaced "wash-out" zones trending NW-SE and NE-SW, clearly visible in both maps correspond to the edges of reprocessed seismic surveys, where geological information was obscured by and removed with uncertain events along survey edges due to filtering. When comparing the definition of discontinuities across the study area in Figure 7, the effect of data quality on the results of attribute analysis and consequently, the final fault map, becomes immediately obvious. In the area of the Central Graben, where the basement is buried at a few kilometres depth (Fig 5 and Fig. 9 a and b) and salt diapirs and walls distort the geometries of the underlying horizons, the fault patterns seem to have a less continuous and, in places, more chaotic character (Fig. 7 b, NE corner). Similarly, lower data quality onshore West Netherlands does not allow highly reliable mapping of the faults (Fig. 7 d, SE corner) using the workflow proposed in this study. Otherwise, the obtained fault maps provide fault information based on good to excellent data quality, which is clearly visible in sections in Figure 9.

Figure 7 here

Fiure. 8 here

Figure 9 here

5.2. Structural trend analysis in the SNS

From the initial impression of the fault maps in Figures 7 and 8 the basement structure of the SNS is far from homogeneous. While some parts of the mapped area show very similar fault patterns, other have a diametrically different character. The overall fault trend, as per the rose diagram in Figure. 8, is NW-SE. Faults trending in 120°-150° azimuth range make up approximately 35% of all faults in the area and including NNW-SSE and WNW-ESE directions (azimuth range between 110° and 160°) – already about 51%. While this number is quite significant, the remaining half follow directions outside of this azimuth range. Perpendicular to the main basement trend there is a second mode NE-SW trend direction of lower magnitude, which contributes only about 16% to the overall population of faults (in the wide azimuth range 20° – 70°). The importance of this and other more local basement structural trends becomes clearer when categorized according to strike direction in a map view as shown in Figure 10 a. The faults in the map and the rose diagram were color-coded according to strike direction to reflect four SNS basement trend directions specified by Stewart & Coward (1995) (refer to Fig. 1 a). Some general observations can be made based on this representation. Firstly, the NW-SE trend (green faults) can be observed across the entire SNS area but its importance decreases from SW to NE. This gradual change is very clear in Figure 11, where the western and southern sub-basins, such as Sole Pit High, Silverpit Basin, Indefatigable Shelf, Broad Fourteens Basin and West Netherlands Basin are characterized by very similar fault trend distributions, with the WNW-ESE to NNW-SSE trend (roughly 110° – 160°) contributing to around 60% of all mapped faults. The dominance of the NW-SE trend can be clearly observed in inset maps d and e in Figure 10. These faults are characterized by high continuity and parallelism over large distances. Figure 10 b depicts a regional transition from highly parallel NW-SE fault systems to more rhomboidal patterns and a higher share of near-N-S and W-E directions.

Figure 10 here

Figure 11 here

The second mode NE-SW trend (navy blue) is important semi-regionally in the areas of the Central Graben, the Central Offshore Platform and the SE edge of the Cleaver Bank High. Especially in the latter two areas this trend is represented by regularly spaced parallel fault systems continuous over distances of several to a few 10's of km. These highly parallel trends correspond largely to 'Dekeyser' faults. They are likely to be underrepresented in the map close to the Cleaver Bank High-Central Offshore Platform boundary due to presence of survey boundaries and associated wash-out zones. An increase of share of the NE-SW trend from Cleaver Bank High to the Central Graben and Central Offshore Platform can be observed in the rose diagrams for those sub-basins in Figure 11. In the eastern part of the study area, in Terschelling Basin and Ameland Platform, there is a strong W-E trend, which clearly dominates over other fault systems in the area. While W-E trending faults can be observed locally in small clusters across the entire SNS (e.g. areas in the immediate vicinity of the South Hewett Fault, Fig. 10 d) as well as towards the W-E trending Mid-North-Sea High. Only in the eastern part of the study area the W-E faults have a truly dominant character. The rose diagram computed for this area strongly contrasts with the rest of the SNS, including all adjacent sub-basins, where the W-E trends can be considered insignificant. Similarly, the N-S basement fault trend has a more local character. N-S faults can be observed predominantly in the NE part of the study area. They show the largest continuity towards the northern margin of the SNS basin, especially on the highs surrounding the Central Graben, in particular, the Mid-North-Sea High, the Schill Ground High and partly the Cleaver Bank. For the former two, this dominant N-S trend is well depicted in Figure 11. It must be considered that the 3D seismic data coverage in these two areas is limited and the overall trend distribution for entire sub-basins may differ.

Central Graben and Ameland Platform are also characterized by an increased share of the N-S trend.

6. Discussion

6.1. Mapping confidence

To better understand the impact of the overlying salt structures on the mapping results, an additional study was done on a subset of the MegaSurvey dataset to compare the trend distribution beneath salt structures and the adjacent salt withdrawal depocenters. The subset consisted of four seismic surveys of good to excellent seismic data quality located withing the boundary of the orange polygon shown in Figure 2. The area was selected to include both concordant and discordant salt structures oriented at various angles to the underlying basement faults. The study consisted in analysing fault trends separately inside and outside of the outlines of existing salt structures. The results were plotted on rose diagrams for comparison. Figure 12 and 13 show the results of the fault mapping and trend analysis.

Figure. 12 here

Figure. 13 here

As evident from the similarity map (Fig. 12a and c), in the presence of salt, edge detection alone does not provide clear structural information, which would be easy to use by the interpreter. Fault enhancement allows resolving more detail, also beneath the salt, as evident from insets c and d in Figure 12. It can be observed that in general the continuity of faults across the salt structures is good, especially where the salt structures are narrow. Wide discordant and concordant structures partly obscure the pre-salt structural information and in places some information is lost or dimmed. Additionally, sinuosity of faults mapped underneath sinuous discordant salt structures may not be fully reliable and may be partly related to salt velocity pull-ups. Despite these potential mapping issues, comparative rose diagrams computed beneath salt structures (Fig. 13 c) and beneath the surrounding depocenters (Fig. 13 d) show a similar trend distribution with the dominant NW-SE direction and a secondary NE-SW direction. This implies that the method generally provides reliable results suitable for analysing pre-salt structural trends.

This analysis was done on a high-quality seismic data set therefore, it can be assumed that the reliability of results will correlate with the data quality, which is especially true at great depths, like in the area of the Central Graben, where the basement is buried at depths of a few kilometres. The fault trend distribution in such areas should be used with care.

6.2. New results vs. published maps

The regional fault maps in Figures 7, 8 and 10 are the first fault map data sets with a semi-detailed resolution derived using a consistent method from a supra-regional merged seismic dataset for the entire area of the Southern North Sea Basin with sufficient local resolution for comparative studies in the future. These fault maps and fault trend analysis in Figure 11 provided new details of the SNS basement structure, which are not accounted for in generalized maps available in the literature. Figure 14 shows a comparison between published structural maps (Fig. 14 a-b) and the results of this study (Fig. 14 c-d), all limited in extent to the size of the area shown in Figure 1c. The published maps clearly show a strong bias towards the NW-SE direction in the Silverpit Basin-Cleaver Bank High area, partly due to the use of 2D seismic data for structural interpretation and partly due to generalization of structural information in the map. The study results in Figure 14 c-d replicate the same general pattern as maps from the literature but they provide more detail, especially in the direction perpendicular to the main structural trends, showing abundant W-E and SW-NE link-ups, which contribute to strong basement segmentation.

Figure. 14 here

At a larger scale, the NW-SE bias in published maps becomes very clear. Figure 15 shows a published regional fault set mapped at the base-of-Zechstein (e.g. Duin et al., 2006, Peryt et al., 2010, ten Veen et al., 2012)cropped to the extent of the MegaSurvey dataset. The rose diagram computed for this fault set shows a very strong NW-SE trend present in the majority of the area which is only occasionally interrupted by faults trending in a different direction. NW-SE fault strikes (in azimuth range 110°-160°) represented in the map contribute to about 73% of all faults inside the polygon. The perpendicular NE-SW trend (20°-70°), quite evident in Figure 10 f, contributes to less than 5% of the total fault data in Figure 15. The NE-SW trend is therefore highly underrepresented in a generalized map although it is included in the central and NE part of the area representing regional Central Graben fault trends.

Figure. 15 here

The W-E trend is only partly represented offshore NE Netherlands but it is not accounted for in the N part of the Silverpit Basin and Cleaver Bank High, where its presence is evident from Figure 10 a. Finally, the importance of the N-S trend in the Schill Ground High area, especially clear from Figure 11, is not captured.

Regional changes in basement trends, easily traceable in the directional trends shown by the rose diagrams in Figure 11 may represent the structural inheritance/grain of smaller pre-Caledonian terranes forming Avalonia. The boundaries of these terranes would not correspond exactly to the present-day boundaries of the SNS sub-basins as marked changes in observed trends in some cases do not at sub-basin boundaries. A good example is the Cleaver Bank High, where three distinct areas characterized by different trends and fault patterns can be found. These are: rhomboidal fault patterns in the NE, parallel NW-SE trends in the W and NE-SW trends in the SE part. Moreover, in the Southern North Sea Basin there is a very strong similarity between trends in the W and SW sub-basins (West Netherlands Basin, Sole Pit High, Cleaver Bank High, Indefatigable Shelf, SW part of the Cleaver Bank High) despite their different tectonic histories. This characteristic may imply their joint origin. The area of the occurrence of the SW-NE trend extending into the Central Graben, Schill Ground High, Mid-North Sea High fragment, Central Offshore Platform and SE part of Cleaver Bank High, may also indicate a genetic link between them however, due to lower quality of results and a limited dataset for some of those sub-basins, the correlations between these areas are not entirely clear. Finally, the Terschelling Basin and Ameland Platform sub-basins are clearly correlated and stand out from the rest of the area as a hypothetical separate unit.

7. Conclusions

This study provides a comprehensive analysis of pre-salt fault trends in the SNS basin. The obtained results are based on a high-detail fault network mapped on the entire study area in a consistent way, using automatic methods, which include 3D seismic attribute analysis and automatic raster tracing, which are free from interpreter bias. The fault maps confirm general trend directions mapped previously by other authors but due to use of 3D seismic, they provide additional details of the basement fault patterns and trend distribution. The results clearly show very strong similarities between sub-basins in the SW part of the study area despite the fact that these sub-basins have gone through different tectonic evolutions. This may imply a joint origin of these sub-basins prior to Caledonian accretion of the Laurussian continent.

The methods selected to track faults in the 3D seismic dataset have proven useful to map discontinuities below salt structures. Despite data quality issues in the Central Graben area and offshore W Netherlands, the majority of results can be treated as reliable. Using an automatic approach for fault mapping allowed obtaining detailed results on a supra-regional 3D seismic dataset in a relatively short amount of time.

Acknowledgements

We thank Oil and Gas Authority (OGA) and Petroleum Geo-Services for providing the 3D MegaSurvey seismic data set used in this study. We also thank software providers: Esri® (ArcMap™), IHS Markit (Kingdom™) and Schlumberger (Petrel™) for use of their software as part of the Royal Holloway academic licence agreement. Moreover, we thank the Institute of Geosciences, University of São Paulo in Brazil for making the Open Stereo available as Free and Open Source Software.

We would also like to thank Dr Ian Watkinson from the Department of Earth Sciences at Royal Holloway, University of London, for a constructive discussion of the validation and uncertainty aspects of the fault mapping workflow.

Appendices

Appendix 1 – Similarity map of the SNS pre-salt basement

Figure A1 here

Appendix 2 – Computer programs listing

- ArcGIS 10.3 for Desktop, Copyright © 1999-2014 Esri:
    - ArcMapTM, trademark of Esri®, version 10.3.0.4322.
- Kingdom 2015.0 – 64-bit, Copyright © 1993-2015 IHS Global Inc. All rights reserved. Build 2426, 23.09.2015:
    - 2D/3DPAK® and EarthPAK®, trademarks of IHS Markit,
    - Rock Solid AttributesTM, trademark of Petroleum GeoServices.
- OpenStereo 0.1.2 devel, Copyright © Carlos H. Grohmann and Ginaldo A.C. Campanha, Institute of Geosciences, University of São Paulo, Brazil
- Petrel 2016.4 – 64-bit, Copyright © 2017 Schlumberger. All rights reserved. Build I4965, 28.09.2017

References

Antrett, P., A. A. Vackiner, P. A. Kukla, S. Back and H. Stollhofen (2012). "Controls on reservoir compartmentalization of an Upper Permian tight gas field in Germany and links to a modern analogue in the Western US." Petroleum Geoscience **18**(3): 289-304.

Ashraf, U., H. Zhang, A. Anees, H. Nasir Mangi, M. Ali, Z. Ullah and X. Zhang (2020). "Application of Unconventional Seismic Attributes and Unsupervised Machine Learning for the Identification of Fault and Fracture Network." Applied Sciences **10**(11): 3864.

Bahorich, M. S. and S. L. Farmer (1995). "3-D seismic coherency for faults and stratigraphic features." The Leading Edge **14**: 1053-1058.

Besly, B. M. (1998). Carboniferous. Petroleum Geology of the North Sea: Basic Concepts and Recent Advances. K. W. Glennie, Blackwell Science Ltd**:** 104-136.

Brown, A. R. (2011). Interpretation of Three-Dimensional Seismic Data, AAPG.

Chopra, S. and K. J. Marfurt (2007). Seismic Attributes for Prospect Identification and Reservoir Characterization, Society of Exploration Geophysicists.

Cohen, I., N. Coult and A. A. Vassiliou (2006). "Detection and extraction of fault surfaces in 3D seismic data." Geophysics **71**(4): P21-P27.

de Jager, J. (2007). Geological development. Geology of the Netherlands. W. Th.E., B. D.A.J. and d. J. J., Royal Netherlands Academy of Arts and Sciences**:** 5–26.

Dorigo, M., V. Maniezzo and A. Colorni (1996). "Ant system: optimization by a colony of cooperating agents." IEEE Transactions on Systems, Man, and Cybernetics, Part B (Cybernetics) **26**(1): 29-41.

Duin, E. J. T., J. C. Doornenbal, R. H. B. Rijkers, J. W. Verbeek and T. E. Wong (2006). "Subsurface structure of the Netherlands - results of recent onshore and offshore mapping." Netherlands Journal of Geosciences - Geologie en Mijnbouw **85**(4): 245-276.

Gersztenkorn, A. and K. J. Marfurt (1999). "Eigenstructure- based coherence computations as an aid to 3-D structural and stratigraphic mapping." Geophysics **64**(5): 1468-1479.

Glennie, K. W. (1990). Outline of the North Sea History and Structural Framework. Introduction to the Petroleum Geology of the North Sea, Blackwell Scientific Publications**:** 34-77.

Glennie, K. W. and J. R. Underhill (1998). Origin, Development and Evolution of Structural Styles. Petroleum Geology of the North Sea: Basic Concepts and Recent Advances. K. W. Glennie, Blackwell Science Ltd**:** 42-84.

Hale, D. (2012). Fault surfaces and fault throws from 3D seismic images. SEG Technical Program Expanded Abstracts 2012**:** 1-6.

Harding, R. and M. Huuse (2015). "Salt on the move: Multi stage evolution of salt diapirs in the Netherlands North Sea." Marine and Petroleum Geology **61**: 39-55.

Laake, A. W., M. S. Sheneshen, C. Strobbia, L. Velasco and A. Cutts (2011). "Integration of surface/subsurface techniques reveals faults in Gulf of Suez oilfields." Petroleum Geoscience **17**(2): 165-179.

Marfurt, K. J. and T. M. Alves (2015). "Pitfalls and limitations in seismic attribute interpretation of tectonic features." Interpretation **3**(1): SB5-SB15.

Marfurt, K. J., R. L. Kirlin, S. L. Farmer and M. S. Bahorich (1998). "3-D seismic attributes using a semblance-based coherency algorithm." Geophysics **63**(4): 1150-1165.

Maystrenko, Y. P., U. Bayer and M. Scheck-Wenderoth (2013). "Salt as a 3D element in structural modeling — Example from the Central European Basin System." Tectonophysics **591**: 62-82.

Ojik, K. v., A. Silvius, Y. Kremer and Z. K. Shipton (2019). Fault seal behaviour in Permian Rotliegend reservoir sequences: case studies from the Dutch Southern North Sea. Integrated Fault Seal Analysis. S. R. Ogilvie, S. J. Dee, R. W. Wilson and W. R. Bailey. London, Geological Society. **496**.

Oncken, O., A. Plesch, J. Weber, W. Ricken and S. Schrader (2000). Passive margin detachment during arc-continent collision (Central European Variscides). Orogenic Processes: Quantification and Modelling in the Variscan Belt of Central Europe. W. Franke, Haak, V., Oncken, O., Tanner, D. London, Geological Society Special Publication**:** 199-216.

Oudmayer, B. C. and J. De Jager (1993). Fault reactivation and obligue slip in the Southern North Sea, London, Geological Society of London.

Pedersen, S. I., T. Skov, T. Randen and L. Sønneland (2005). "Automatic Fault Extraction Using Artificial Ants." Mathematical Methods and Modelling in Hydrocarbon Exploration and Production **7**: 107-116.

Peryt, T. M., M. C. Geluk, A. Mathiesen, J. Paul and K. Smith (2010). Zechstein. Petroleum Geological Atlas of the Southern Permian Basin Area. J. C. Doornenbal and A. G. Stevenson. Houten), EAGE Publications b.v.**:** 123-147.

Pharaoh, T. C. (1999). "Palaeozoic terranes and their lithospheric boundaries within the Trans-European Suture Zone (TESZ): a review." Tectonophysics **314**(1): 17-41.

Randen, T., S. I. Pedersen and L. Sønneland (2001). "Automatic detection and extraction of fault surfaces from three-dimensional seismic data." SEG Technical Program Expanded Abstracts 2001: 551-554.

Stewart, S. A. and M. P. Coward (1995). "Synthesis of salt tectonics in the southern North Sea, UK." Marine and Petroleum Geology **12**(5): 457-475.

Tamagawa, T., K. Tezuka and N. Tsuchiya (2012). "Use of a computational fault-extraction process with calibrations to characterize a fractured basement reservoir, Yufutsu, Japan." AAPG Bulletin **96**(12): 2275–2296.

ten Veen, J. H., S. F. van Gessel and M. den Dulk (2012). "Thin-and thick-skinned salt tectonics in the Netherlands; a quantitative approach." Netherlands Journal of Geosciences **91**(4): 447-464.

Wu, X., L. Liang, Y. Shi and S. Fomel (2019). "FaultSeg3D: Using synthetic data sets to train an end-to-end convolutional neural network for 3D seismic fault segmentation." Geophysics **84**(3): IM35-IM45.

Ziegler, P. A. (1990a). Geological Atlas of Western and Central Europe. Bath, Geological Society Publishing House.

Ziegler, P. A. (1990b). Tectonic and palaeogeographic development of the North Sea rift system. Tectonic evolution of the North Sea rifts. D. J. Blundell, Gibbs, A.D., Oxford Science Publications. **81**.

Table of figures

Figure 1: Structural maps from the Southern North Sea area showing different level of structural detail at the base-of-Zechstein: a) major basement trends in the SNS, modified after Stewart & Coward (1995); b) TWT structure map with variance attribute showing detailed fault pattern and salt velocity pull-up effect on fault definition below salt structures. Four main salt structures marked with letters A-D. Modified after Harding & Huuse (2015), location shown in d; c) semi-detailed fault pattern in the Cleaver Bank High area after Oudmayer & de Jager (1993), location shown in d; d) major faults at base-of-Zechstein horizon, modified after Peryt et al. (2010). Extent of seismic dataset used in this study shown for reference as blue polygon

Figure 2: Location map with salt extent and dataset limits. TB - Terschelling Basin, AP – Ameland Platform. Salt extent after Maystrenko et al. (2013)

Figure 3: Chronostratigraphic chart for the Southern North Sea Basin, modified after Stewart and Coward (1995)

Figure 4: Examples of the quality of seismic imaging of the SNS MegaSurvey 3D seismic data; a) Silverpit Basin characterized by relatively shallow depths, mild basement deformation, generally thick salt and gradual changes of salt thickness, little faulting in the salt overburden; very good imaging of the entire section allows low-uncertainty structural interpretation and horizon mapping b) Central Graben characterized by larger depths, strong basement deformation, abundance of salt walls and diapirs and high level of deformation in the post-salt overburden; the quality of imaging suddenly decreases below and around salt structures, which distort underlying reflectors due to sharp contrast in seismic velocities, making the interpretation in this area more challenging. Note: data is in the European polarity.

Figure 5: Base-of-Zechstein TWT map. Limit of Zechstein salt shown with magenta line after Maystrenko et al. (2013). Map modified from regional interpretation provided by Petroleum Geo-Services.

Figure 6: Fault mapping methodology

Figure 7: Ant tracking attribute map of base-of-Zechstein horizon calculated in the Petrel software on a similarity map; Note very good definition of faults in general, with results uncertainty increasing for onshore data (bottom-right corner of d) as well as for large depths, intensive diapirism and high structural complexity (b). Limit of Zechstein salt after Maystrenko et al. (2013)

Figure 8: Basement trends mapped on base-of-Zechstein horizon. The rose diagram shows an overall basement fault trend distribution. The diagram is weighted by lengths of individual fault segments. Limit of Zechstein salt after Maystrenko et al. (2013)

Figure 9: Regional cross-sections from the study area showing very complex structural architecture between different sub-basins: a) SW-NE-ENE section across the study area, capturing NW-SE and N-S basement fault trends; b) NW-SE section across the Central Graben, showing NE-SW trending faults in the Central Graben area. Locations of cross-sections shown on map and in Fig. 2.

Figure 10: Fault distribution map of the base-of-Zechstein horizon. Full extent of mapped horizon is shown in a. Inset maps b-e illustrate in detail fault patterns mapped in various areas of the basin. Rose diagram in inset f shows a fault trend analysis for all faults mapped in a. The colours used for faults in maps a-e correspond to colours used for different strike azimuths in the rose diagram in inset f. Limit of Zechstein salt after Maystrenko et al. (2013)

Figure 11: Distribution of basement fault trends by sub-basin. Limit of Zechstein salt after Maystrenko et al. (2013)

Figure 12: Base salt: a) similarity map (Kingdom software); b) ant tracking map (Petrel software); c) similarity map zoom-in; d) ant tracking map zoom-in. Salt structure outlines are shown on ant tracking maps for reference. Better resolution of discontinuities around and underneath salt structures can be observed on the ant tracking map (b, d) as compared to similarity map (a, c). Location shown in Fig. 2.

Figure 13: Fault trend analysis: a) fault distribution map (ArcMap software) showing faults traced using automatic vectorization, color-coded according to strike direction; b) fault map zoom-in. Salt structures shown in pink for reference; rose diagrams: c) faults traced below salt structures, d) faults traced below depocenters surrounding salt structures, limited in extent to c. 20 km from salt structures, e) all traced faults. Rose diagrams (OpenStereo software) are weighted by lengths of individual fault segments. Observations include: similar orientation patterns below and away from salt structures, largely oblique to overlying salt structures; slightly bimodal fault strike distribution. Location shown in Fig. 2.

Fig. 14: Comparison between published maps and study results, limited to the extent of the area mapped in Oudmayer and de Jager (1993). Location shown in Fig. 2; a) major basement trends at base of Zechstein horizon, modified after Peryt et al. (2010), b) semi-detailed fault pattern mapped using partly 2D data, after Oudmayer & de Jager (1993), c) ant tracking attribute map, d) fault tracing result

Figure 15: Analysis of basement trends based on published regional map in Peryt et al. (2010). Limit of Zechstein salt after Maystrenko et al. (2013)

Figure A1: Similarity attribute map of base-of-Zechstein horizon calculated in the Kingdom software; Note presence of elongated zones of blurred image (low similarity values) caused by salt velocity pull-ups of the horizon below salt structures. Limit of Zechstein salt after Maystrenko et al. (2013)

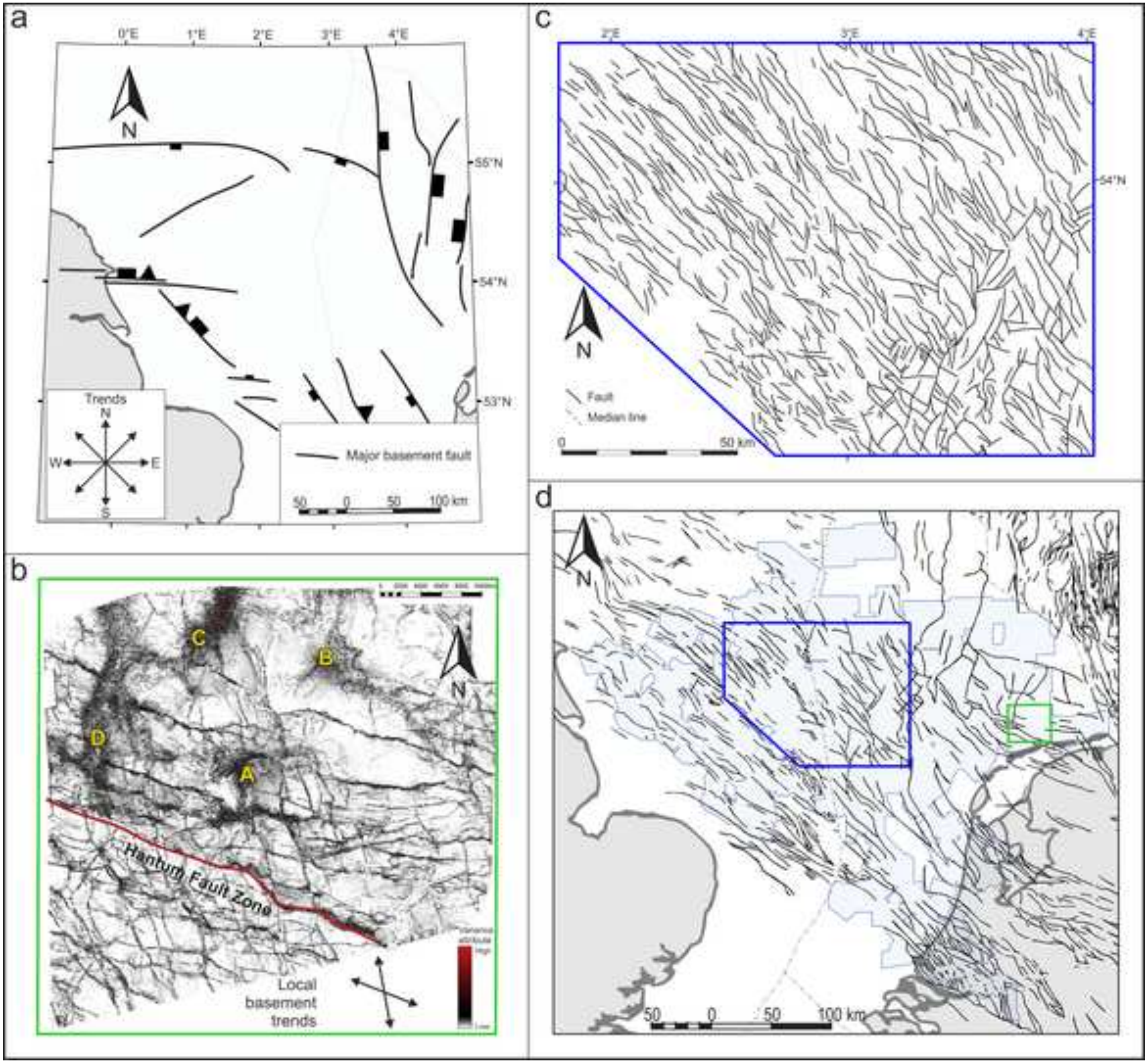
a
0°E
1°E
2°E
3°E
4°E
N
55°N
54°N
53°N
Trends
N
W
E
S
Major basement fault
50
0
50
100 km
b
C
B
D
A
N
Hantum Fault Zone
Local
basement
trends
c
2°E
3°E
4°E
54°N
N
Fault
Median line
0
50 km
d
N
50
0
50
100 km

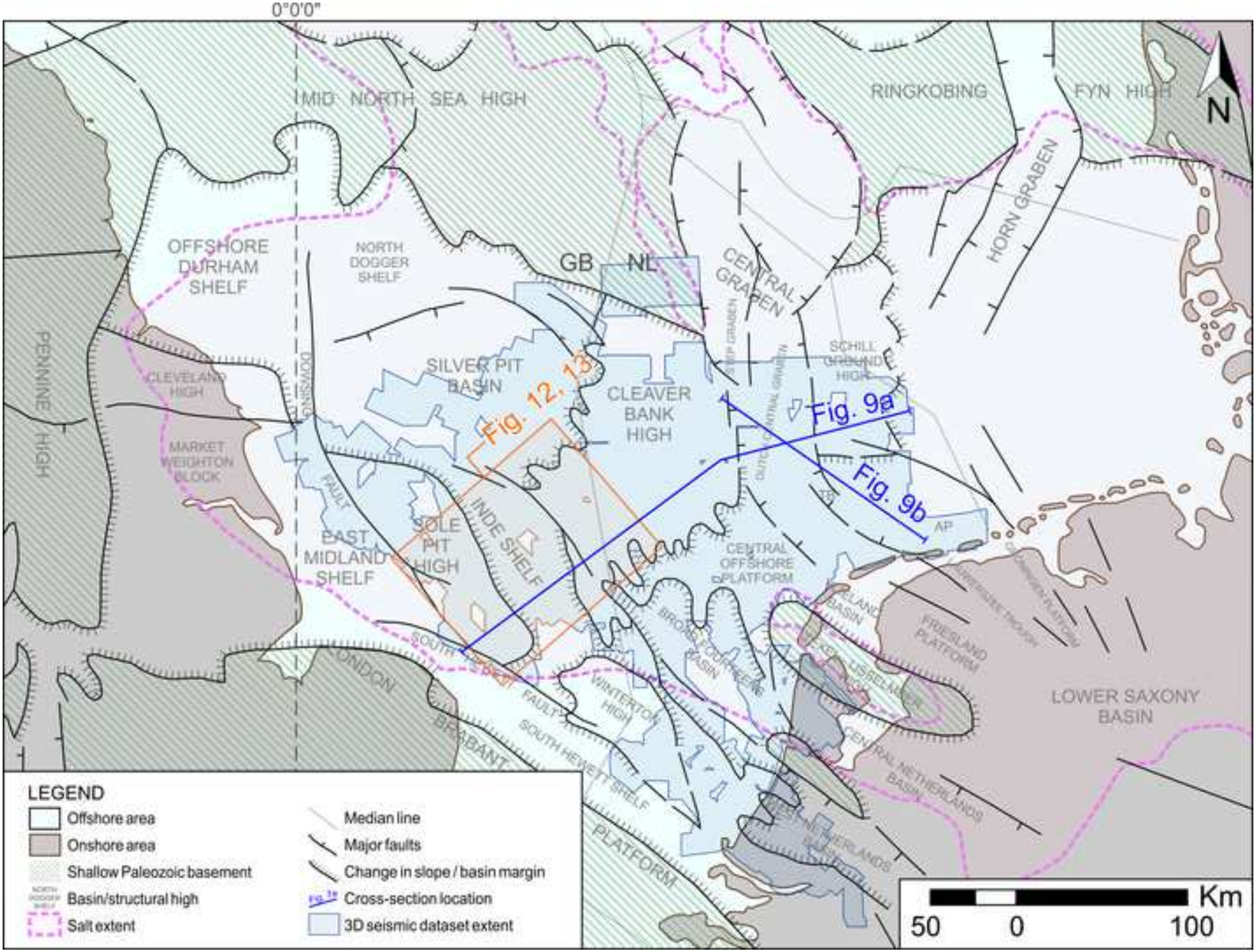
0°0'0"
MID NORTH SEA HIGH
RINGKOBING
FYN HIGH
N
OFFSHORE DURHAM SHELF
NORTH DOGGER SHELF
GB
NL
CENTRAL GRABEN
HORN GRABEN
PENNINE HIGH
CLEVELAND HIGH
DOWSING
SILVER PIT BASIN
Fig. 12, 13
CLEAVER BANK HIGH
SCHILL GROUND HIGH
DUTCH CENTRAL GRABEN
Fig. 9a
Fig. 9b
TB
AP
MARKET WEIGHTON BLOCK
FAULT
EAST MIDLAND SHELF
SOLE PIT HIGH
INDE SHELF
CENTRAL OFFSHORE PLATFORM
BROAD FOURTEENS BASIN
FRIESLAND PLATFORM
LAUWERSZEE TROUGH
GRONINGEN PLATFORM
IJSSELMEER
LOWER SAXONY BASIN
SOUTH
LONDON
BRABANT
FAULT
WINTERTON HIGH
SOUTH HEWETT SHELF
PLATFORM
CENTRAL NETHERLANDS BASIN
NETHERLANDS BASIN
LEGEND
Offshore area
Onshore area
Shallow Paleozoic basement
NORTH DOGGER SHELF
Basin/structural high
Salt extent
Median line
Major faults
Change in slope / basin margin
Fig. 1a
Cross-section location
3D seismic dataset extent
Km
50
0
100

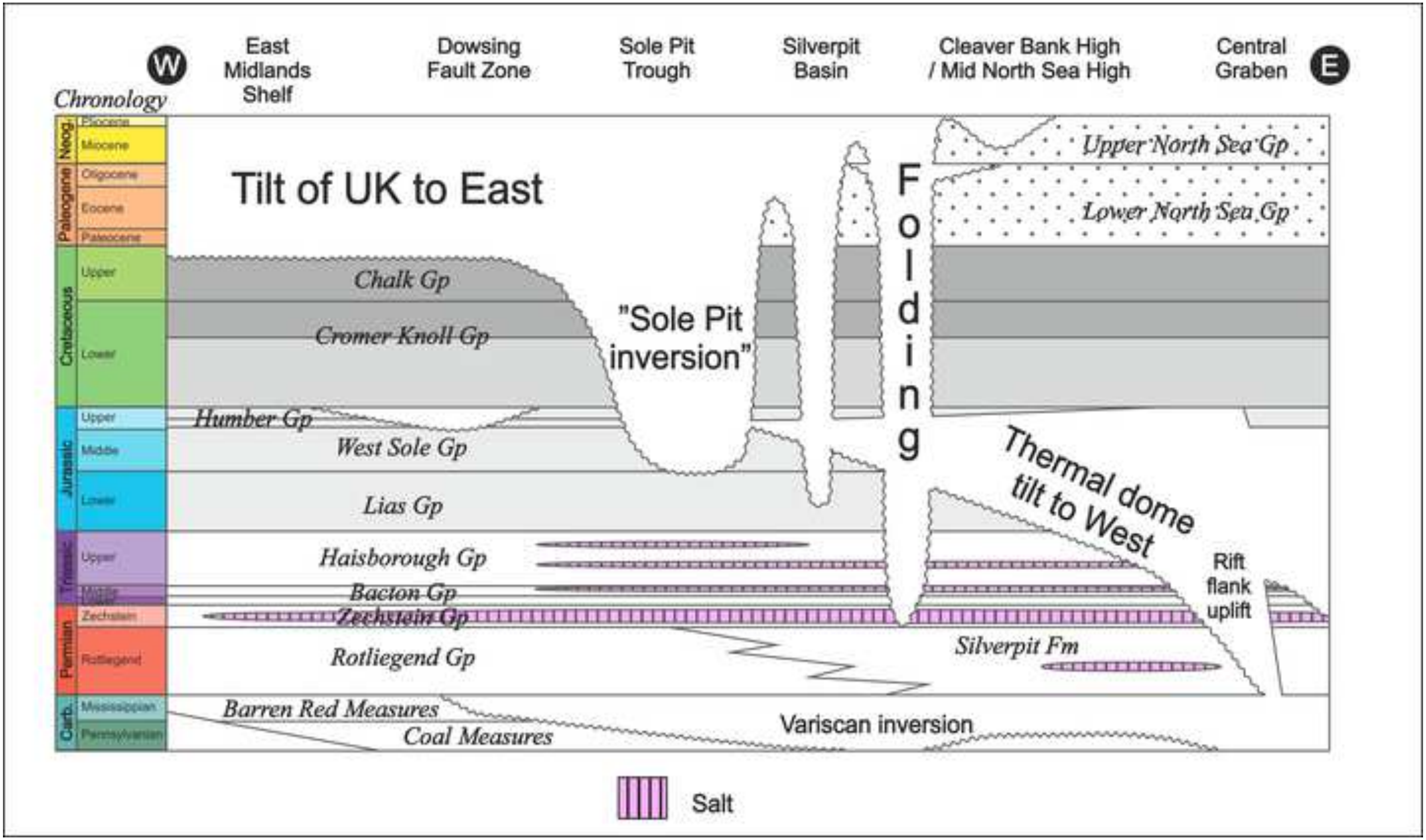
W
East Midlands Shelf
Dowsing Fault Zone
Sole Pit Trough
Silverpit Basin
Cleaver Bank High / Mid North Sea High
Central Graben
E
Chronology
Neog.
Pliocene
Miocene
Paleogene
Oligocene
Eocene
Paleocene
Cretaceous
Upper
Lower
Jurassic
Upper
Middle
Lower
Triassic
Upper
Middle
Lower
Permian
Zechstein
Rotliegend
Carb.
Mississippian
Pennsylvanian
Tilt of UK to East
Upper North Sea Gp
Lower North Sea Gp
Chalk Gp
Cromer Knoll Gp
"Sole Pit inversion"
Folding
Humber Gp
West Sole Gp
Lias Gp
Thermal dome tilt to West
Haisborough Gp
Bacton Gp
Zechstein Gp
Rift flank uplift
Rotliegend Gp
Silverpit Fm
Barren Red Measures
Coal Measures
Variscan inversion
Salt

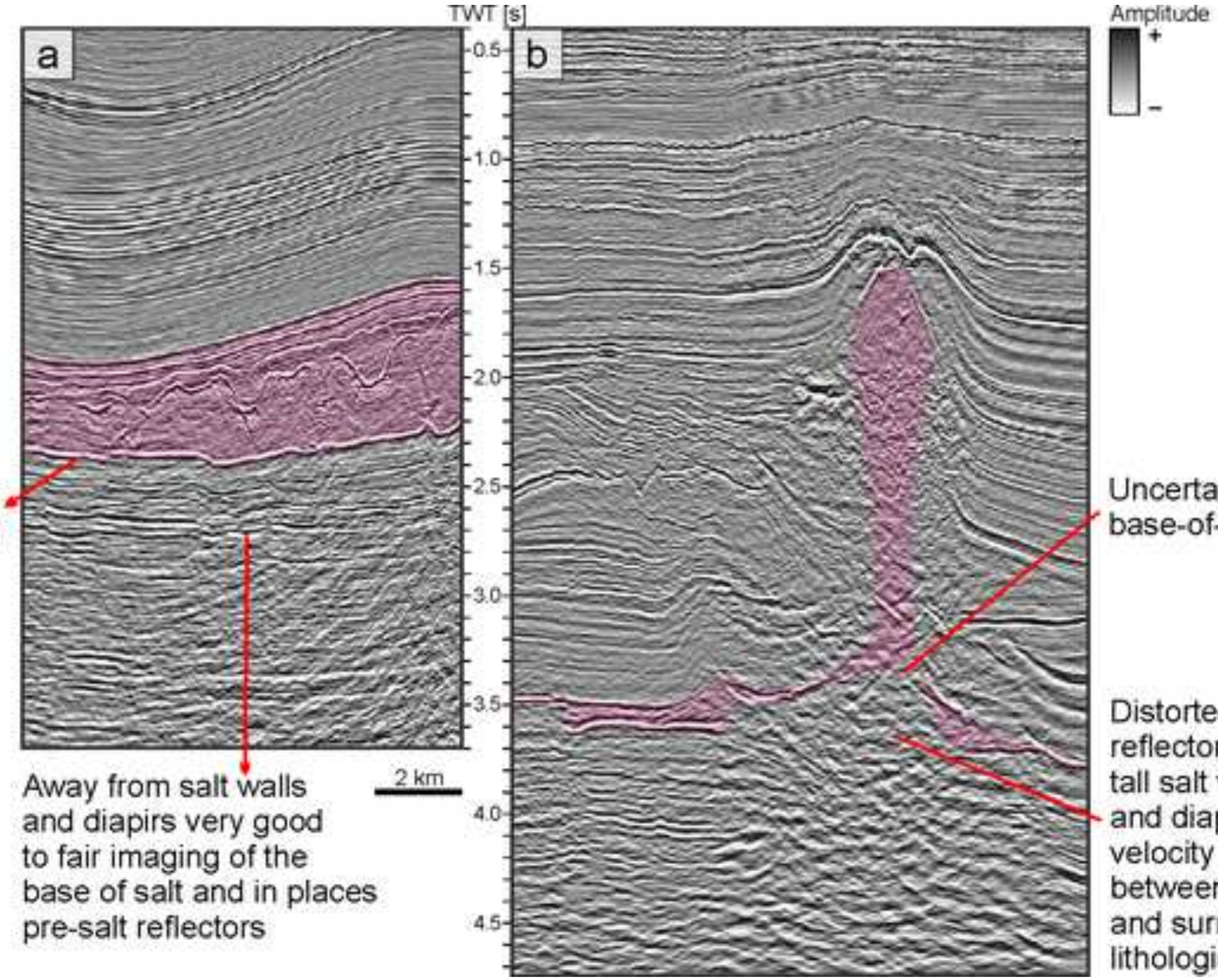

Easily mappable base-of-salt horizon

Away from salt walls and diapirs very good to fair imaging of the base of salt and in places pre-salt reflectors

Uncertainty in mapping base-of-salt horizon

Distorted pre-salt reflectors below tall salt walls and diapirs due to velocity contrast between salt and surrounding lithologies

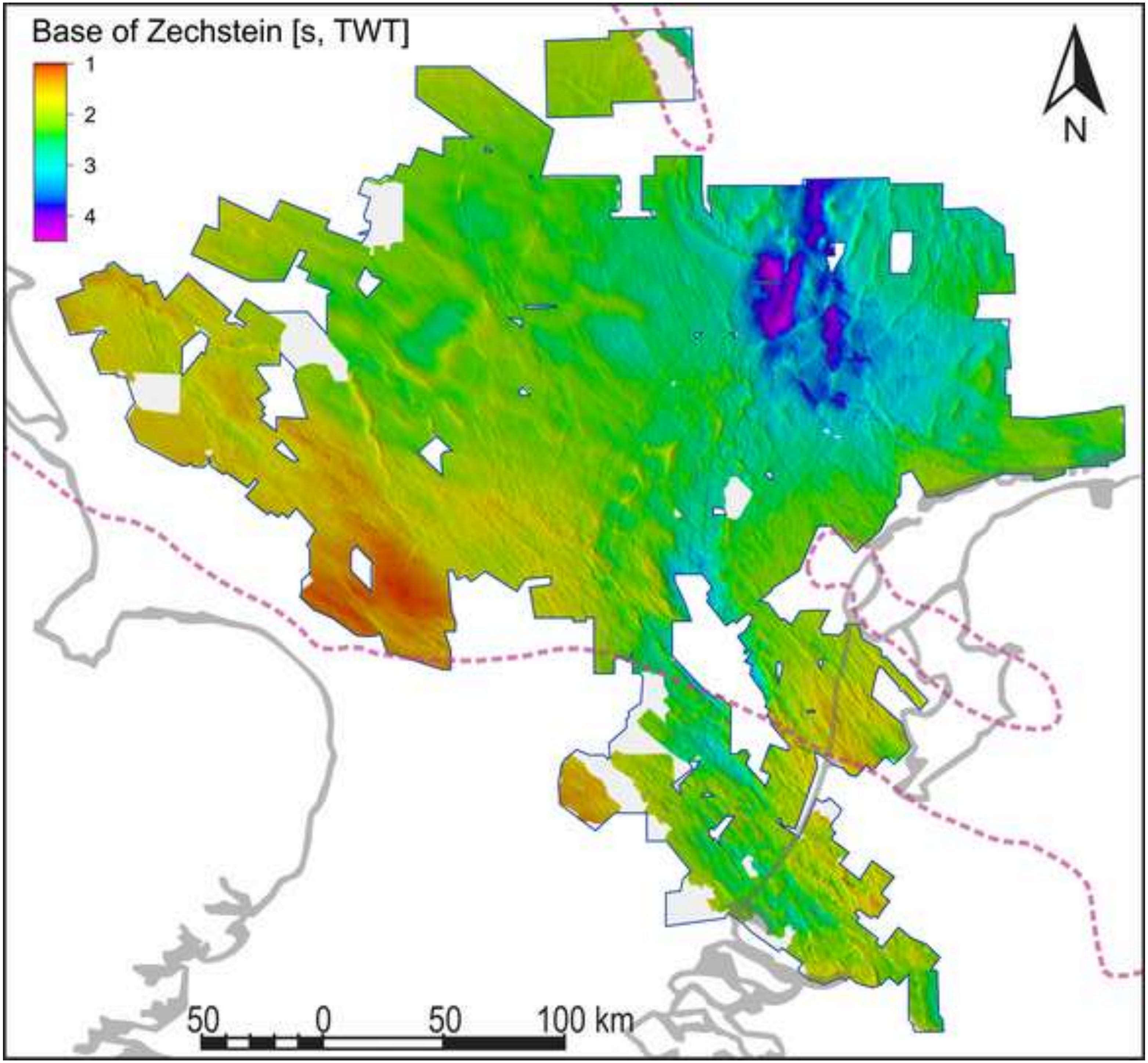
Base of Zechstein [s, TWT]
1
2
3
4
N
50
0
50
100 km

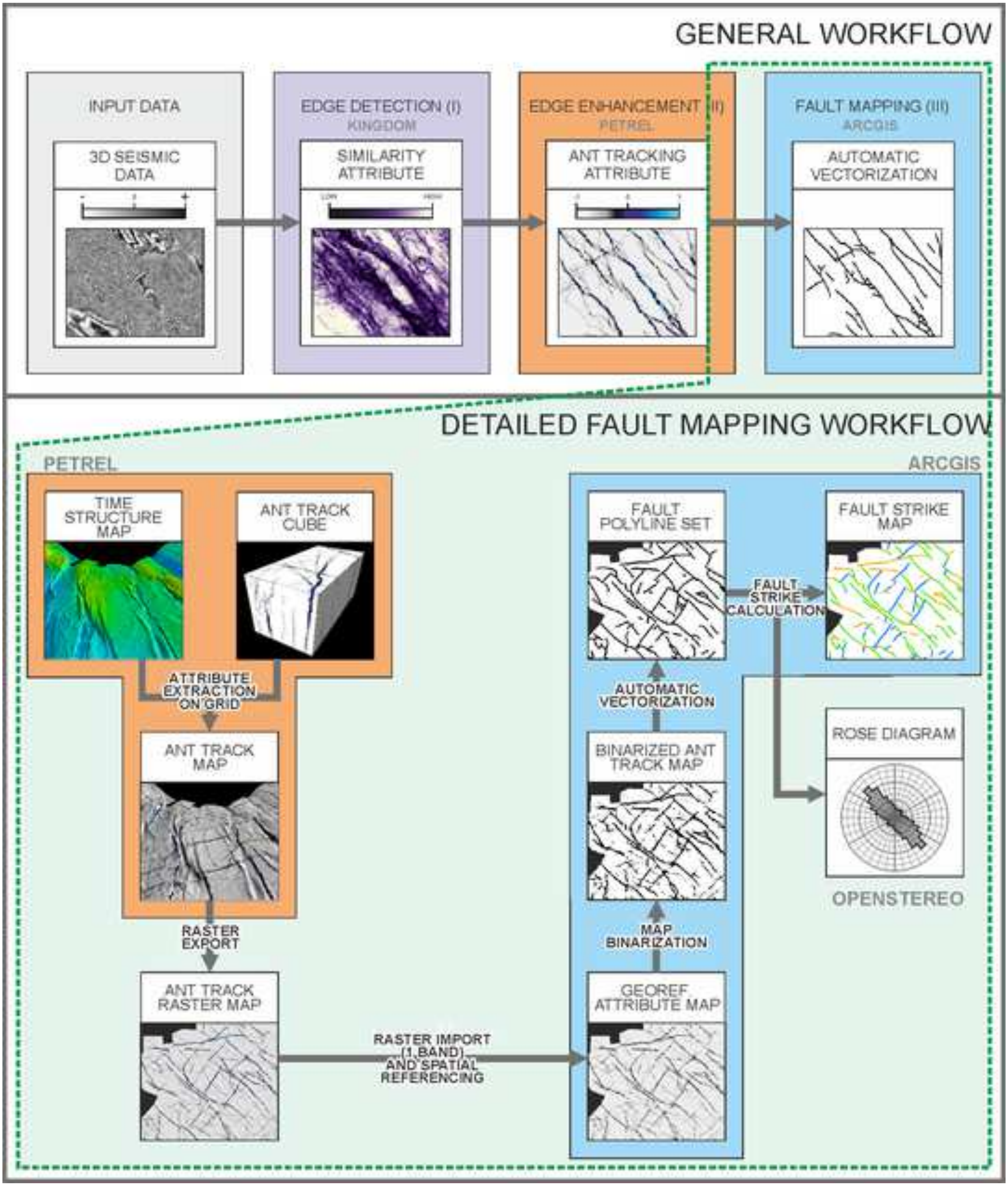
GENERAL WORKFLOW
INPUT DATA
3D SEISMIC DATA
EDGE DETECTION (I)
KINGDOM
SIMILARITY ATTRIBUTE
LOW
HIGH
EDGE ENHANCEMENT (II)
PETREL
ANT TRACKING ATTRIBUTE
FAULT MAPPING (III)
ARCGIS
AUTOMATIC VECTORIZATION
DETAILED FAULT MAPPING WORKFLOW
PETREL
TIME STRUCTURE MAP
ANT TRACK CUBE
ATTRIBUTE EXTRACTION ON GRID
ANT TRACK MAP
RASTER EXPORT
ANT TRACK RASTER MAP
RASTER IMPORT (1 BAND) AND SPATIAL REFERENCING
ARCGIS
FAULT POLYLINE SET
FAULT STRIKE CALCULATION
FAULT STRIKE MAP
AUTOMATIC VECTORIZATION
BINARIZED ANT TRACK MAP
MAP BINARIZATION
GEOREF ATTRIBUTE MAP
ROSE DIAGRAM
OPENSTEREO

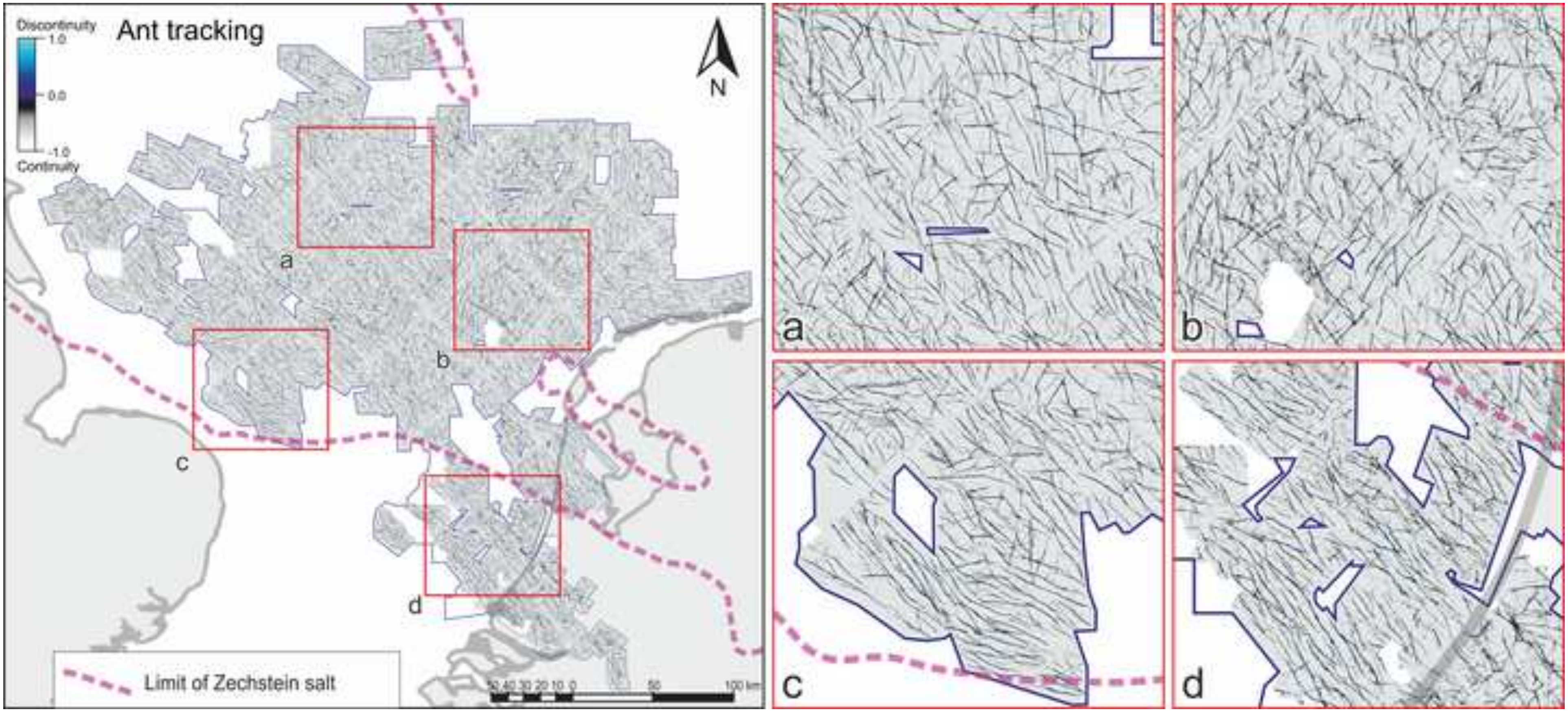
Discontinuity
1.0
0.0
-1.0
Continuity
Ant tracking
N
a
b
c
d
Limit of Zechstein salt
50 40 30 20 10 0 50 100 km
a
b
c
d

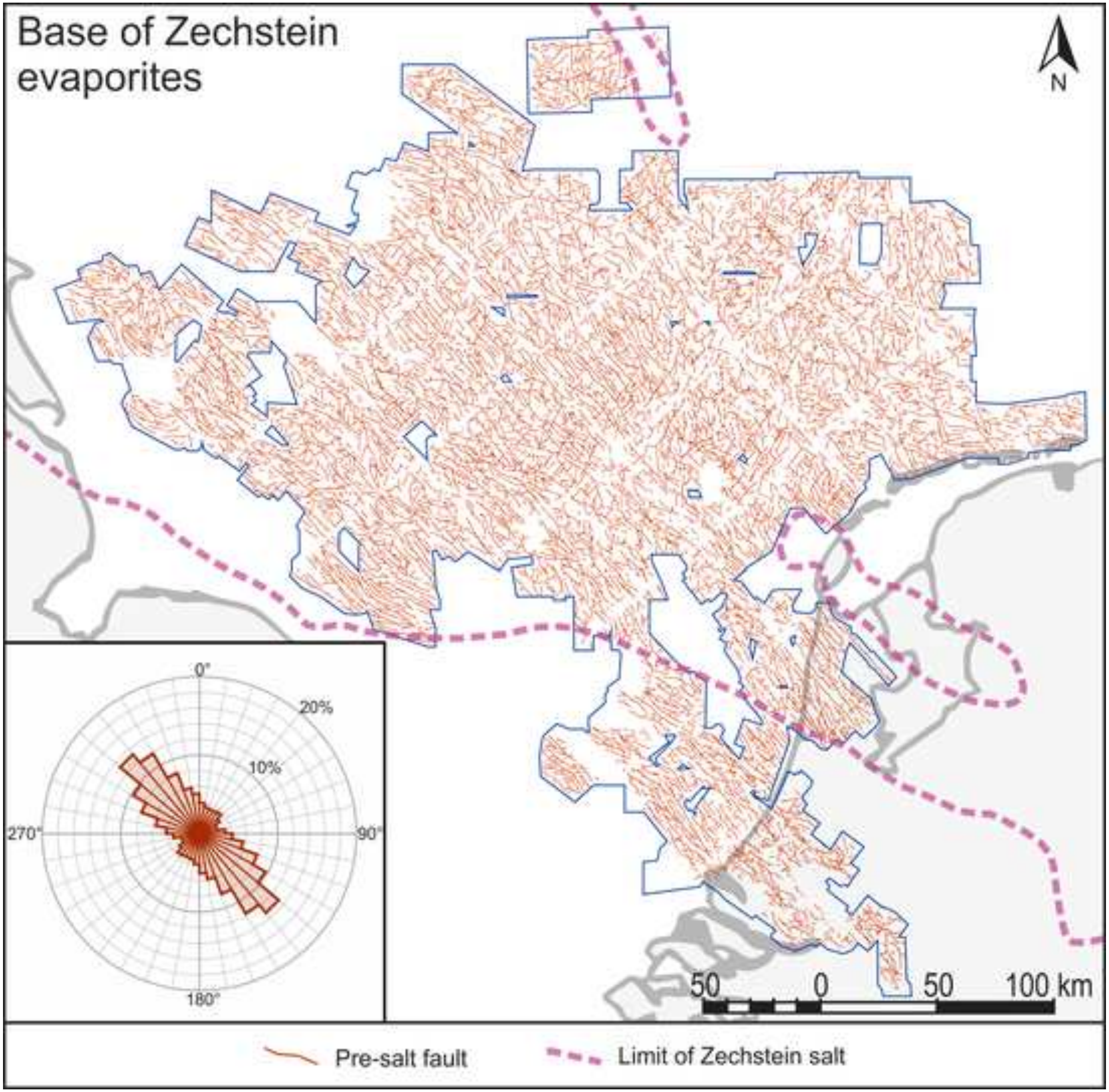
Base of Zechstein evaporites
N
0°
20%
10%
270°
90°
180°
50
0
50
100 km
Pre-salt fault
Limit of Zechstein salt

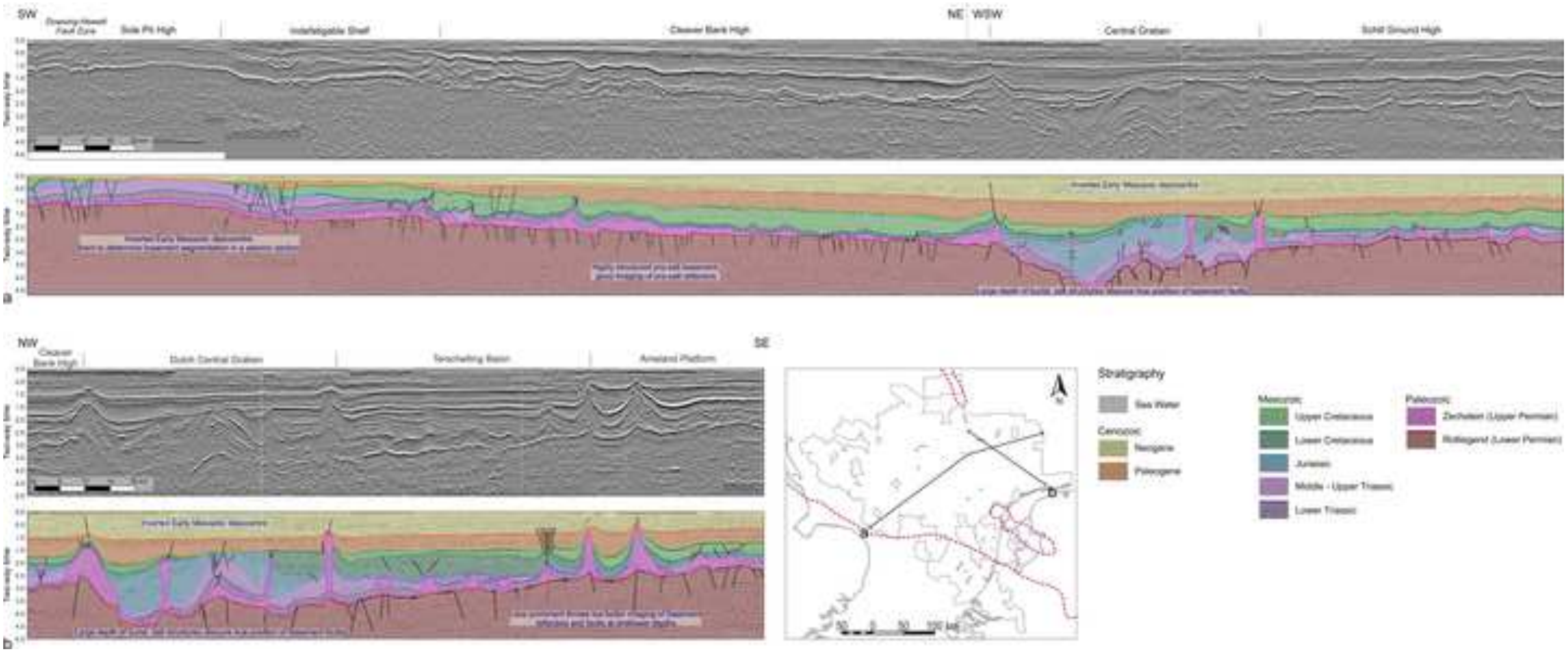
SW
NE
WSW
Sole Pit High
Indefatigable Shelf
Cleaver Bank High
Central Graben
Schill Grund High
Two-way time
a
NW
SE
Cleaver Bank High
Dutch Central Graben
Terschelling Basin
Ameland Platform
b
Stratigraphy
Sea Water
Cenozoic
Neogene
Paleogene
Mesozoic
Upper Cretaceous
Lower Cretaceous
Jurassic
Middle - Upper Triassic
Lower Triassic
Paleozoic
Zechstein (Upper Permian)
Rotliegend (Lower Permian)
N
50
0
50
100 km

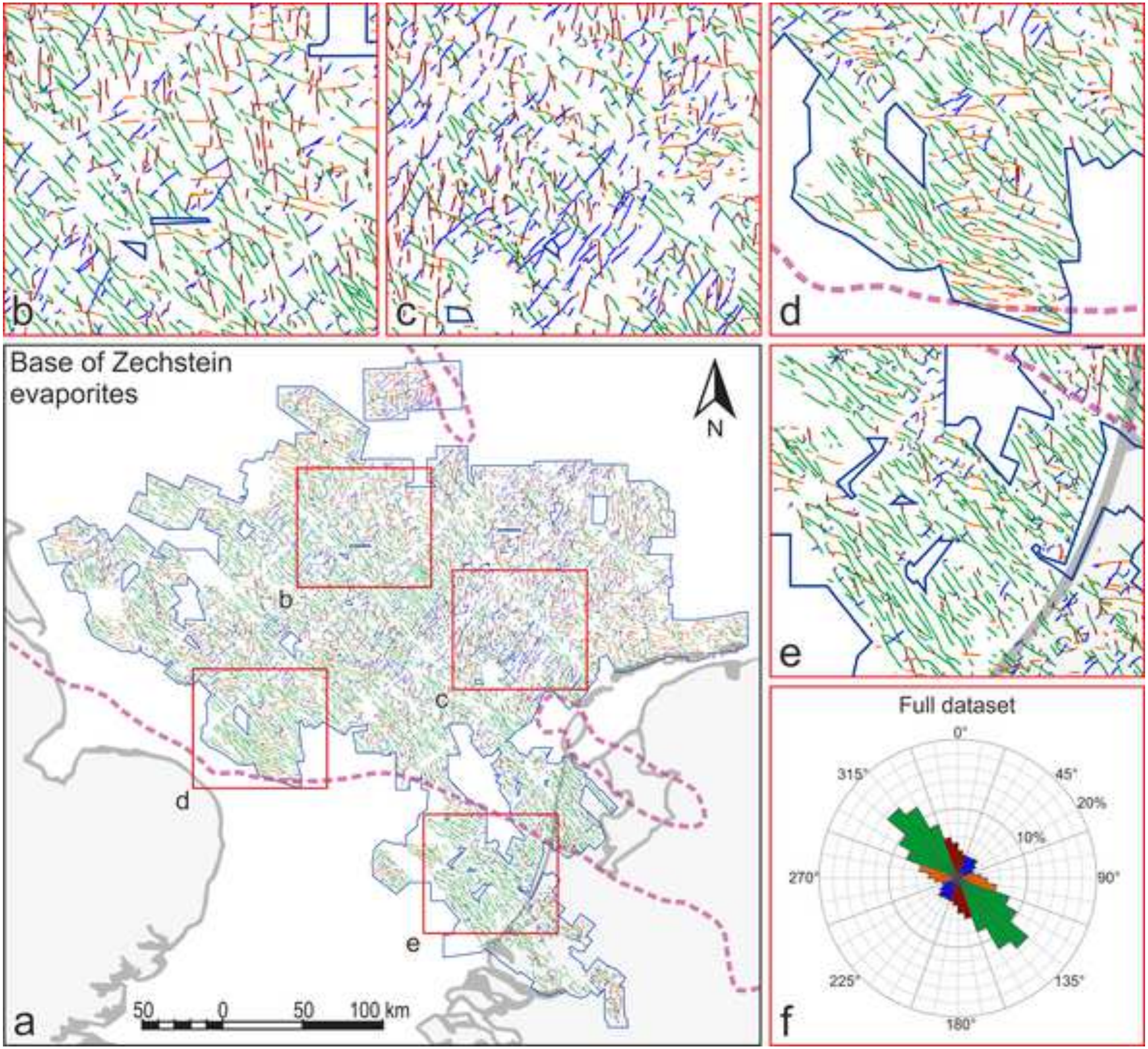
b
c
d
Base of Zechstein evaporites
N
b
c
d
e
a
50 0 50 100 km
e
Full dataset
0°
45°
20%
10%
90°
135°
180°
225°
270°
315°
f

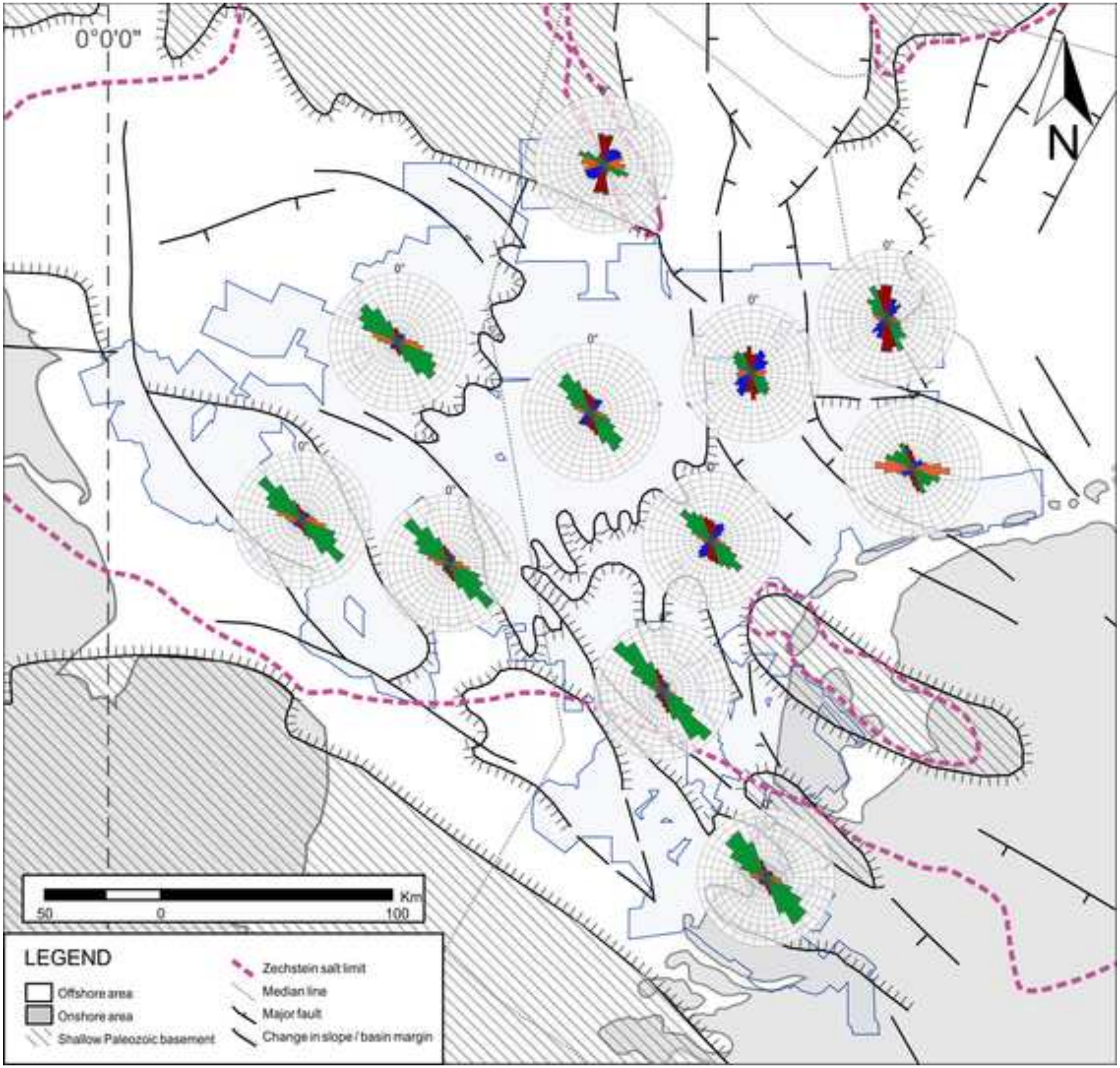
0°0'0"
N
0°
50
0
100
Km
LEGEND
Offshore area
Onshore area
Shallow Paleozoic basement
Zechstein salt limit
Median line
Major fault
Change in slope / basin margin

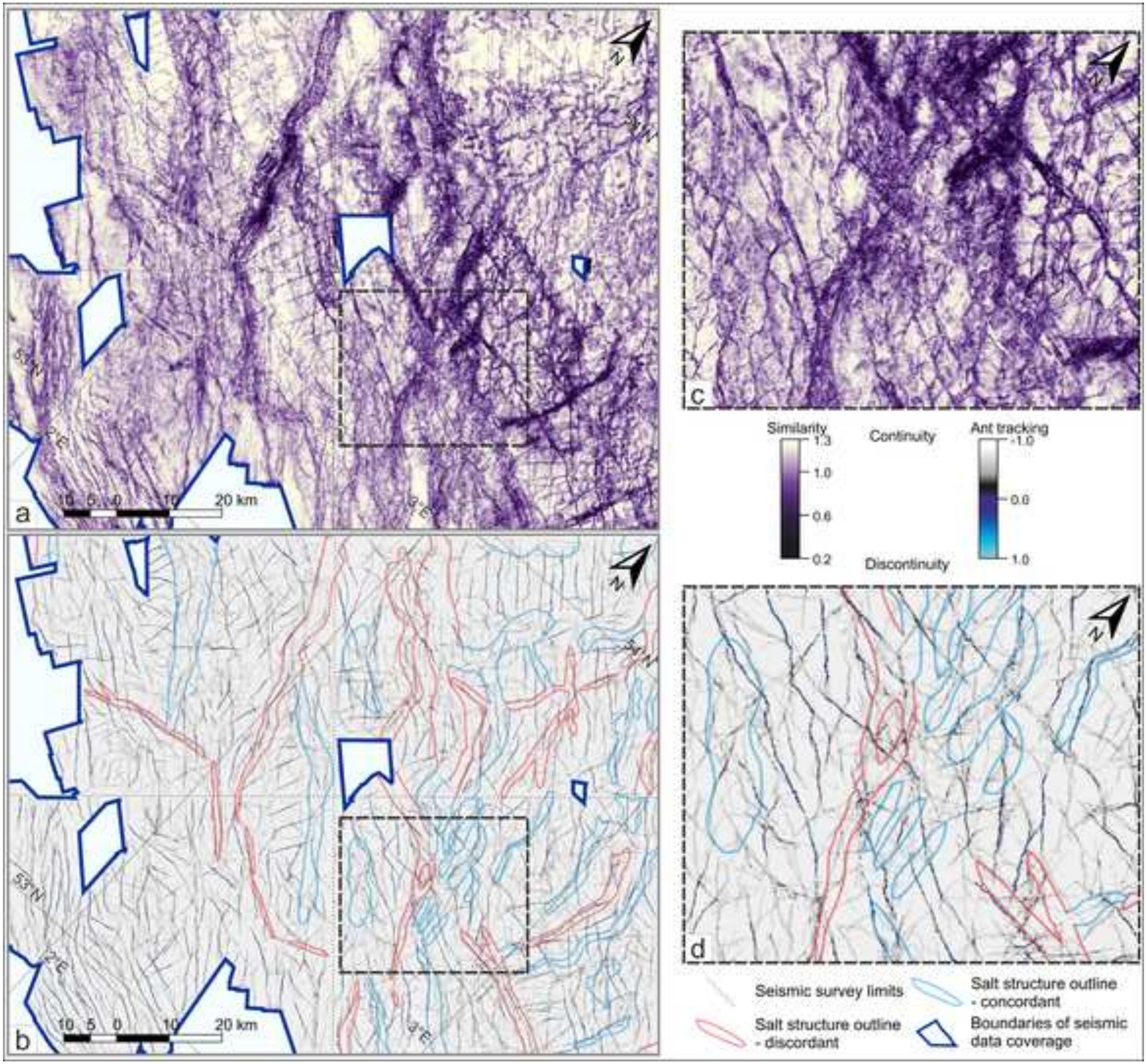
a
b
c
d
N
53°N
54°N
2°E
3°E
10 5 0 10 20 km
Similarity
1.3
1.0
0.6
0.2
Continuity
Discontinuity
Ant tracking
-1.0
0.0
1.0
Seismic survey limits
Salt structure outline - discordant
Salt structure outline - concordant
Boundaries of seismic data coverage

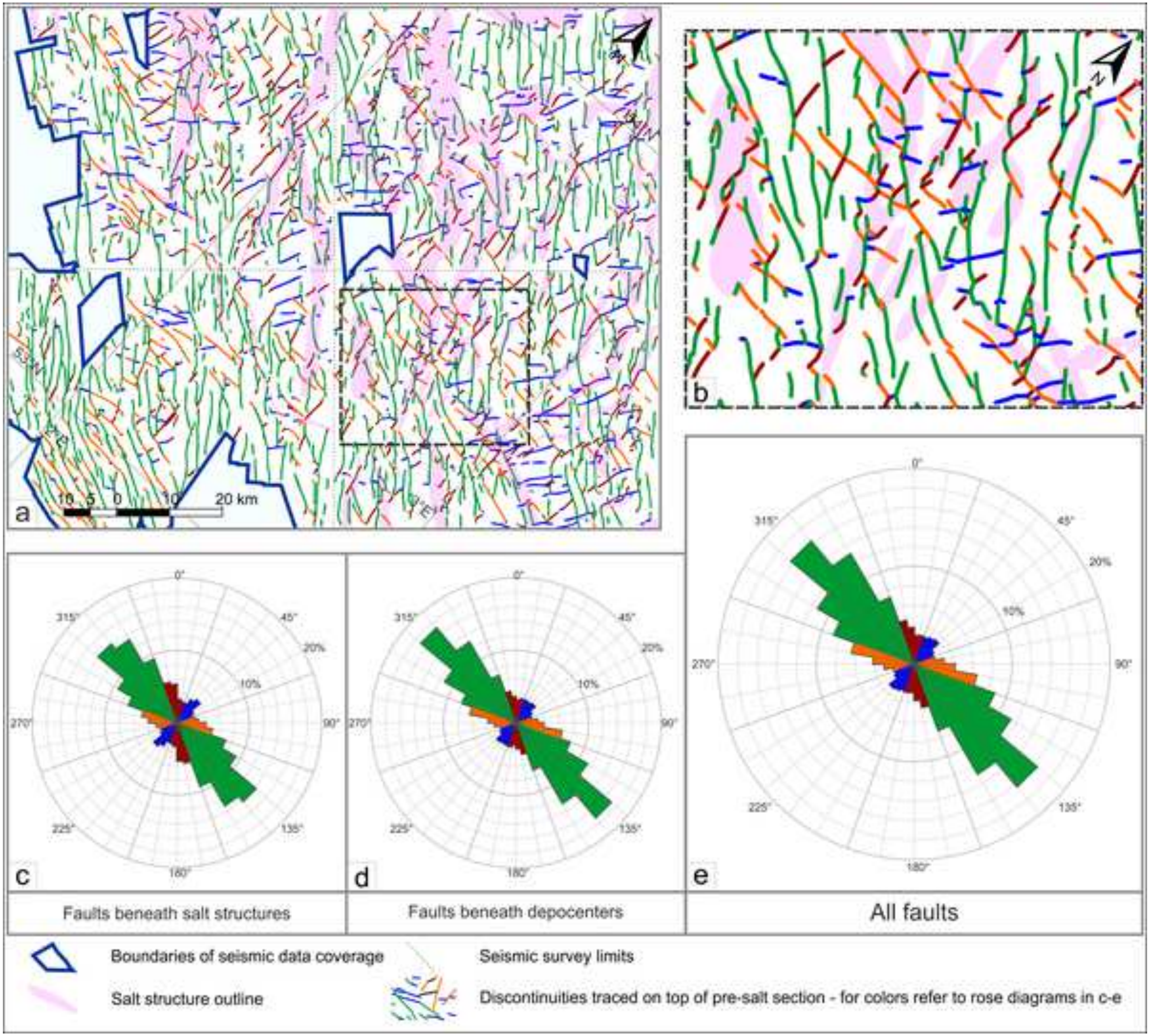
a
N
10 5 0 10 20 km
b
N
c
0°
45°
90°
135°
180°
225°
270°
315°
10%
20%
Faults beneath salt structures
d
0°
45°
90°
135°
180°
225°
270°
315°
10%
20%
Faults beneath depocenters
e
0°
45°
90°
135°
180°
225°
270°
315°
10%
20%
All faults
Boundaries of seismic data coverage
Salt structure outline
Seismic survey limits
Discontinuities traced on top of pre-salt section - for colors refer to rose diagrams in c-e

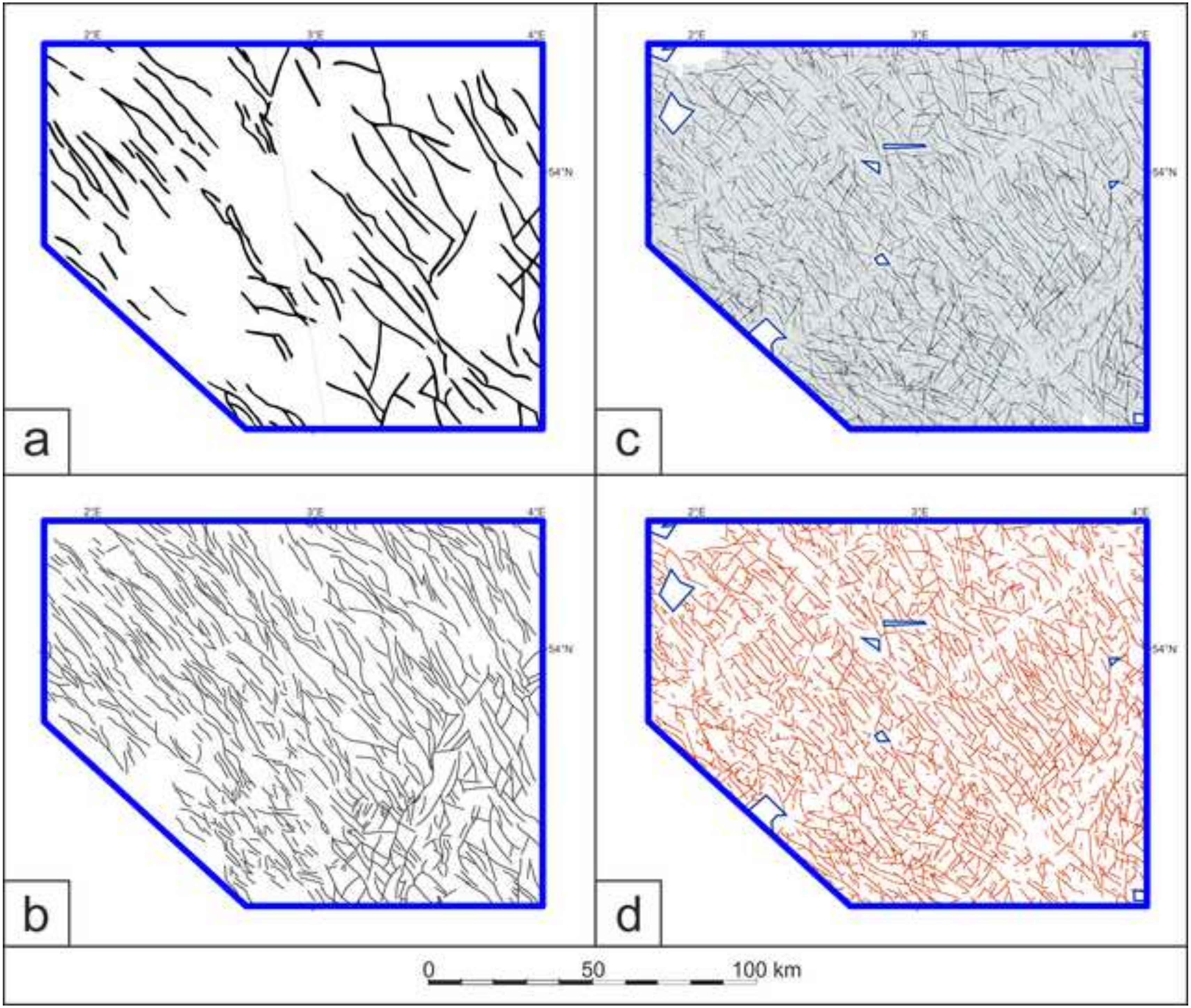
2°E
3°E
4°E
54°N
a
b
c
d
0
50
100 km

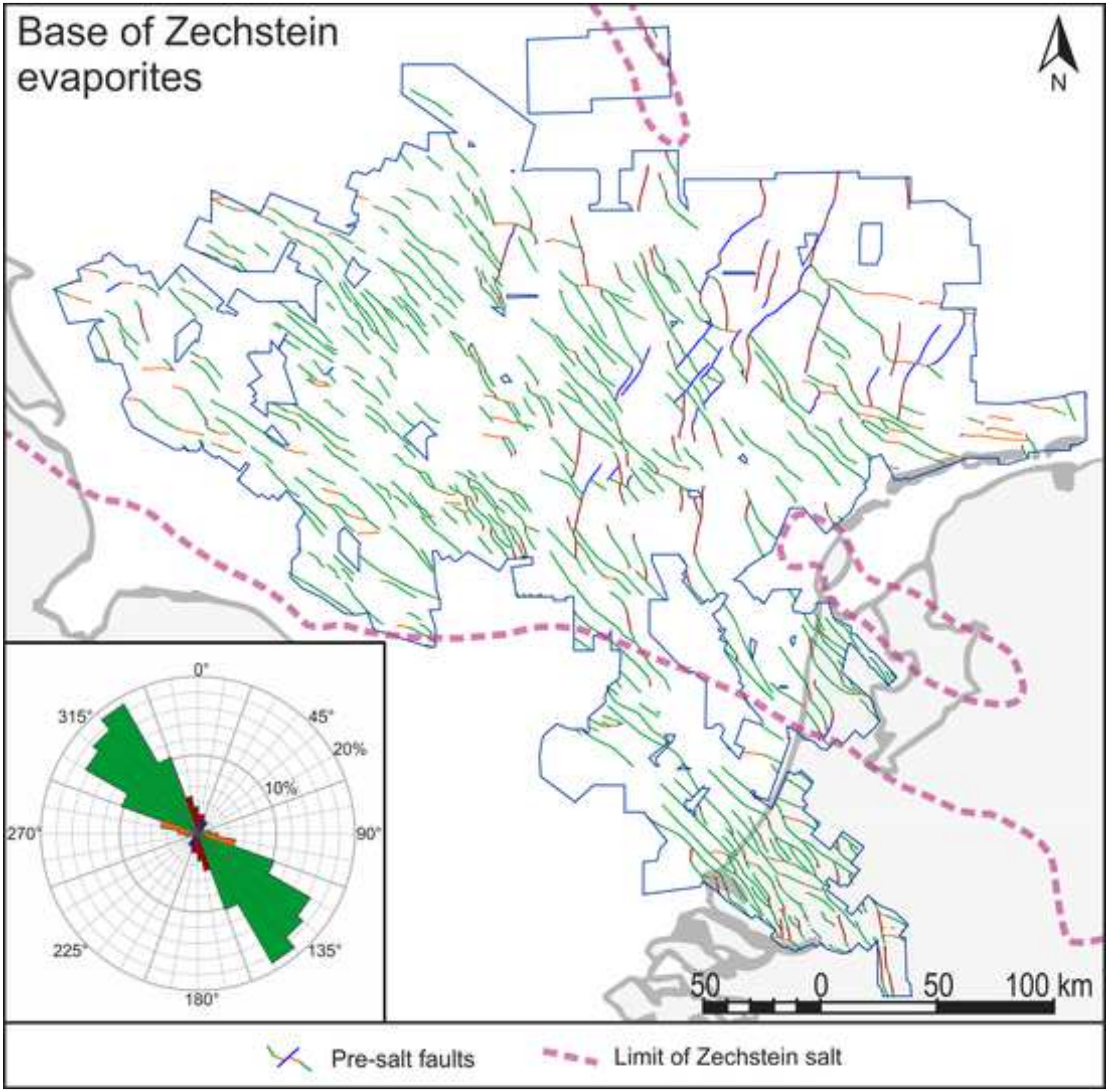
Base of Zechstein evaporites
N
0°
315°
45°
20%
10%
270°
90°
225°
135°
180°
50
0
50
100 km
Pre-salt faults
Limit of Zechstein salt

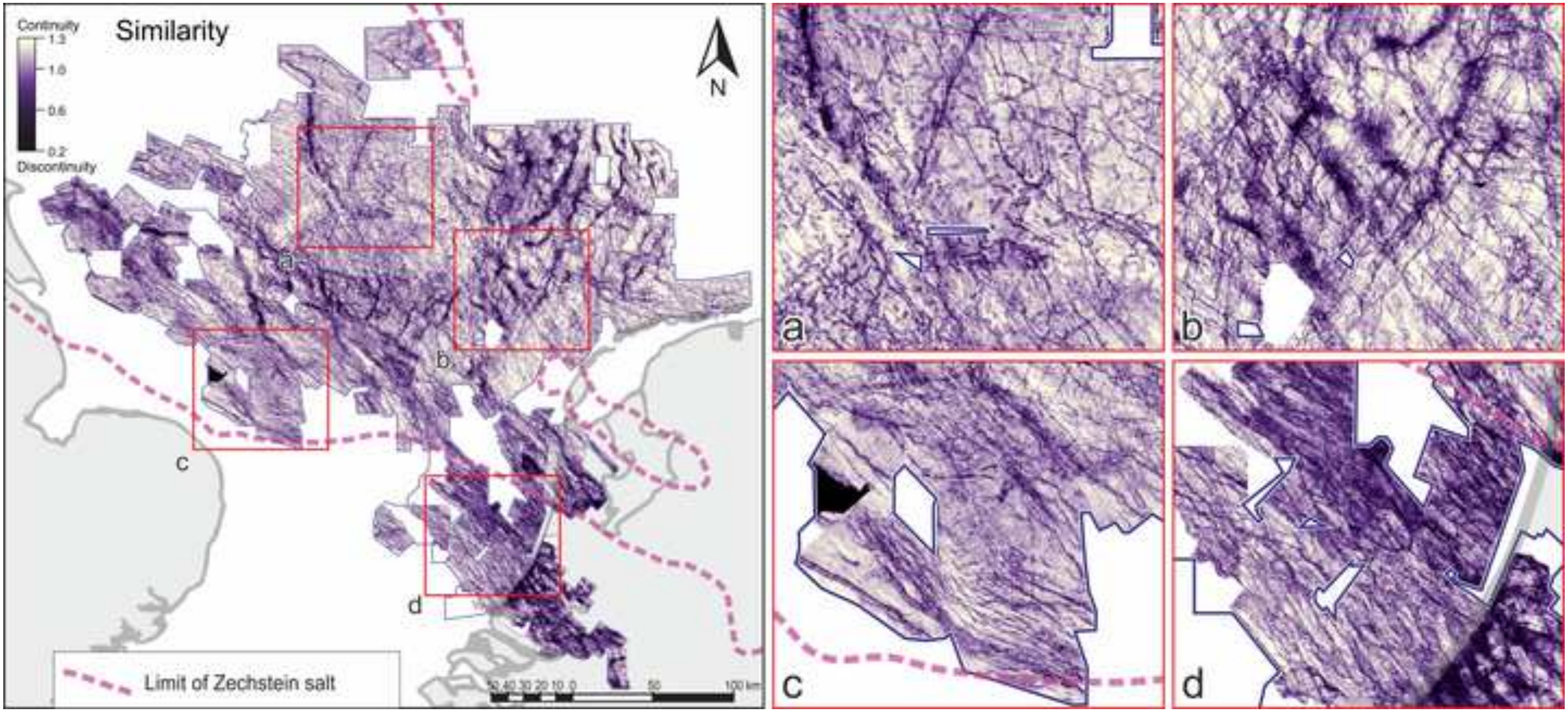
Similarity
Continuity
1.3
1.0
0.6
0.2
Discontinuity
N
a
b
c
d
Limit of Zechstein salt
50 40 30 20 10 0
50
100 km